This is the author accepted manuscript of: Zhou, X., Qiao, D., Macdonald, M., & Li, X. (in press). Optical orbit determination for asteroid approach with vision-based range information. Journal of Guidance, Control, and Dynamics.

Optical Orbit Determination for Asteroid Approach with Vision-based Range Information

Xingyu Zhou* and Dong Qiao†
Beijing Institute of Technology, 100081 Beijing, People's Republic of China

Malcolm Macdonald‡
University of Strathclyde, Glasgow, Scotland G1 1XJ, United Kingdom

Xiangyu Li§
Beijing Institute of Technology, 100081 Beijing, People's Republic of China

Optical measurements are widely used in orbit determination (OD) during the approach phase of an asteroid exploration mission. Optical-only OD suffers from range ambiguity, leading to poor OD performance. This paper proposes a method to improve optical-only OD performance using vision-based range (VBR) measurements. The proposed method doesn't rely on prior knowledge about the shape or size of the asteroid. The proposed method first calculates the asteroid's area projected on the image, with which the ratios of ranges from spacecraft to asteroid between different epochs are obtained. Then, VBR measurements are constructed by multiplying the range ratios and the previous range estimations. A linear programming algorithm is developed to filter noises and improve the accuracy of VBR measurements. Additionally, as the VBR measurement relies on both current and previous states, expressions of the covariance are derived to handle the time-series dependency of VBR measurements, which can improve the accuracy and uncertainty quantification capacity. Finally, optimal estimations are obtained using both the angle and VBR measurements in a Kalman filter framework. The proposed method's performance is validated in the approach phase of the Bennu asteroid. Numerical simulations show that the estimation accuracy and convergence are improved by approximately 37%.

I. Introduction

The last two decades have witnessed an increased interest in asteroid exploration from both scientific and engineering communities [1–4]. As asteroids are remnants of our early solar system, a detailed investigation of their composition can provide deep insight into the origins of life and the formation of the planets. In addition, asteroid exploration is of

*Ph.D. Candidate, School of Aerospace Engineering; zhouxingyu@bit.edu.cn.
†Professor, School of Aerospace Engineering; qiaodong@bit.edu.cn (Corresponding Author).
‡Professor, Department of Electronic and Electrical Engineering; malcolm.macdonald.102@strath.ac.uk. Associate Fellow AIAA.
§Associated Professor, School of Aerospace Engineering; lixiangy@bit.edu.cn.

interest for potential in-situ resource utilization [5, 6]. Various asteroid exploration missions have been implemented, including NEAR Shoemaker [7], Hayabusa2 [8], OSIRIS-REx [9, 10], and AIDA [11, 12].

There are several types of asteroid exploration missions, such as the flyby [3, 13, 14], landing [15, 16], impact [11, 12], and sample return [10, 17]. No matter which type of mission, the approach to the asteroid is an inevitable phase in which the spacecraft needs to find the asteroid, determine orbits, and guide its trajectory toward the asteroid [3, 18, 19]. As an effective orbit determination (OD) method, on-board optical measurements have been widely used in previous asteroid missions [20–23]. It is well-known that the optical measurement approach to OD suffers from drawbacks related to range ambiguity [24, 25]. The approach trajectory with respect to the asteroid is an almost straight line, toward the asteroid. The straight line-like relative trajectory causes the similarity of measurements at different epochs and significantly degrades the performance of optical-only OD [19, 26, 27] The range ambiguity problem of optical measurements can be resolved by constructing additional range measurements. Generally, there are two ways to construct range information: direct and indirect. The direct means is to add an on-board range sensor, such as a Lighting Detection and Ranging (LiDAR) [28, 29], to provide reliable range measurements. However, the on-board range sensor can only work when the spacecraft is close enough to the asteroid (usually tens of kilometers). In addition, a range sensor like LiDAR adds more complexity to the spacecraft, which is inappropriate for small-satellite platforms whose mass and power are limited [22].

An indirect means of constructing range measurement (or measurements related to range information) is by combining optical information with additional information of the target body, such as shape and size (or diameter). Christian proposed a method to navigate a spacecraft using the target body's centroid and apparent diameter in images [30]. The target body is modeled as a triaxial ellipsoid with known sizes, and then the position of the spacecraft relative to the target body can be obtained by fitting the projection of the target body on the image using an ellipse. Recently, Takahashi *et al.* made significant progress in this area by investigating the possibility of using angular size (equivalent to dividing the range by the asteroid's mean radius) measurement to improve optical-only asteroid approach navigation performance [13]. Takahashi's method relies on shape reconstruction methods to accurately model the asteroid's shape [5, 31] and an initial guess of the asteroid's mean radius. In addition, the problem of range ambiguity can be improved if a secondary asteroid exists (say, a binary asteroid system) [32], or the spacecraft executes a maneuver [19]. These methods rely on particular conditions (shape, number of asteroids, or additional maneuvers), which limit their applicability.

This paper proposes a method to improve the performance of in-direct, passive (without additional maneuver), optical-only OD during the asteroid approach phase. The proposed method constructs additional vision-based range (VBR) measurements without prior information (shape or size) about the target asteroid. The VBR measurement of a current epoch is obtained by multiplying the range ratios between the current and previous epochs and the estimated range of the previous epoch. The range ratio is obtained based on the asteroid's area projected on the image plane at different epochs, which are calculated using a subpixel edge detection-based method. In this way, range measurements are obtained without requiring shape or size information of the asteroid. To address the effects of the asteroid's irregular shape on the VBR measurements, a linear programming algorithm is developed to smooth the range ratio data. Additionally, as the VBR measurement is related to both the current and the previous state, new expressions for the cross-correlation covariance matrix and the predicted measurement covariance matrix are derived under the framework of the extended Kalman filter. The newly derived covariance expressions can better handle the time-series dependency of the VBR measurements. The proposed method is applied to solve the OD problem in the approach phase to the asteroid Bennu to validate its performance. The proposed method's accuracy and convergence are tested by comparing it with several competitive methods. Moreover, the sensitivity of the proposed method with respect to the target asteroid's ephemeris error is also investigated and discussed.

The remainder of this paper is organized as follows. The dynamics and measurement models, the standard extended Kalman filter, and the pixel area calculation method are introduced in Sec. II. Section III details the key techniques of the proposed method. Numerical examples are given in Sec. IV, and conclusions are given in Sec. V.

II. System Model & Preliminaries

A. Dynamics and measurement model

A classic OD problem can be represented by a combination of a nonlinear dynamical equation and a measurement equation in the form

$$\begin{cases} \dot{\boldsymbol{x}} = \boldsymbol{f}(t, \boldsymbol{x}) \\ \boldsymbol{z} = \boldsymbol{h}(\boldsymbol{x}) + \boldsymbol{\varepsilon} \end{cases}, \tag{1}$$

where $\boldsymbol{x} = [\boldsymbol{r}; \boldsymbol{v}] \in \mathbb{R}^6$ denotes the state vector of the spacecraft at the epoch t, $\boldsymbol{r} = [x, y, z]^T \in \mathbb{R}^3$ and $\boldsymbol{v} = [\dot{x}, \dot{y}, \dot{z}]^T \in \mathbb{R}^3$ represent the position and velocity vectors of the spacecraft, respectively, $\dot{\boldsymbol{x}} = \boldsymbol{f}(t, \boldsymbol{x}) : \mathbb{R}^6 \mapsto \mathbb{R}^6$ is an ordinary differential equation defining the nonlinear dynamics model, $\boldsymbol{z} \in \mathbb{R}^m$ is the measurement vector, $\boldsymbol{h}(\boldsymbol{x}) \in \mathbb{R}^m$ denotes the measurement model, $\boldsymbol{\varepsilon} \in \mathbb{R}^m$ is the zero-mean white measurement noise and m is the dimension of the measurement model.

The heliocentric equatorial inertial (HEI) frame is employed in this work. It is a fixed reference frame with its origin at the center of the Sun and its x-axis aligned with the mean vernal equinox at 1200hrs Terrestrial Time on 1 January 2000 (*i.e.*, J2000). The dynamic model used herein to describe the motion of the spacecraft includes the point-mass gravity fields of the Sun and perturbation bodies, and the solar radiation pressure (SRP), given by

$$\begin{cases} \dot{\boldsymbol{r}} = \boldsymbol{v} \\ \dot{\boldsymbol{v}} = -\frac{\mu_s}{\|\boldsymbol{r}\|^3}\boldsymbol{r} + \sum\limits_i \mu_i \left(\frac{r_i - r}{\|r_i - r\|^3} - \frac{r_i}{\|r_i\|^3} \right) + C_R \frac{A}{m} P_{\odot} \mathrm{AU}^2 \frac{\boldsymbol{r}}{\|\boldsymbol{r}\|^3} \end{cases}, \tag{2}$$

where μ_s denotes the gravitational constant of the Sun, μ_i and $\boldsymbol{r}_i \in \mathbb{R}^3$ represent the gravitational constant and the position vector (in the HEI frame) of the i-th perturbation body, respectively, C_R stands for the reflection coefficient of the spacecraft, $P_\odot = 4.56 \times 10^{-6}\,\mathrm{N/m^2}$ is the reference value of the SRP at a distance of 1 AU (149597870.0 km) from the Sun and $\frac{A}{m}$ denotes the area-to-mass ratio of the spacecraft. The ephemeris data of the disturbing bodies used herein comes from the Jet Propulsion Laboratory's Development Ephemerides (DE430) [33].

Two measurements are employed: the angle measurement and the vision-based range (VBR) measurement. Therefore, the measurement equation in Eq. (1) can be further written as

$$\boldsymbol{z} = \begin{bmatrix} z_1 \\ z_2 \end{bmatrix} = \boldsymbol{h}(\boldsymbol{x}) + \boldsymbol{\varepsilon} = \begin{bmatrix} \boldsymbol{h}_1(\boldsymbol{x}) + \boldsymbol{\varepsilon}_1 \\ \boldsymbol{h}_2(\boldsymbol{x}) + \boldsymbol{\varepsilon}_2 \end{bmatrix}, \tag{3}$$

where $z_1 = \boldsymbol{h}_1(\boldsymbol{x}) + \boldsymbol{\varepsilon}_1$ and $z_2 = \boldsymbol{h}_2(\boldsymbol{x}) + \boldsymbol{\varepsilon}_2$ represent the angle measurement equation and the VBR measurement equation, respectively. The angle measurement describes the relative direction between the spacecraft and the asteroid. Once the image is taken by equipped optical sensors, the angle information can be obtained by identifying points and streaks in the image and then extracting the targeted asteroid. The angle measurement can be represented by the right ascension α and the declination β, given by

$$\alpha = \tan^{-1}\frac{y_a - y}{x_a - x},\ \beta = \sin^{-1}\frac{z_a - z}{\|\boldsymbol{r}_a - \boldsymbol{r}\|}, \tag{4}$$

where $\boldsymbol{r}_a = [x_a, y_a, z_a]^T \in \mathbb{R}^3$ represents the position vector of the asteroid. The angle measurements are obtained using a moment algorithm called the center-of-mass algorithm [34]. Additionally, the VBR measurement model will be provided in Sec. III.

The corresponding discrete format of the OD problem is formulated as

$$\begin{cases} \boldsymbol{x}_k = \boldsymbol{F}(\boldsymbol{x}_{k-1}, t_{k-1}, t_k) \\ \boldsymbol{z}_k = \begin{bmatrix} z_{1,k} \\ z_{2,k} \end{bmatrix} = \boldsymbol{h}(\boldsymbol{x}_k) + \boldsymbol{\varepsilon}_k = \begin{bmatrix} \boldsymbol{h}_1(\boldsymbol{x}_k) + \boldsymbol{\varepsilon}_{1,k} \\ \boldsymbol{h}_2(\boldsymbol{x}_k) + \boldsymbol{\varepsilon}_{2,k} \end{bmatrix} \end{cases}, \tag{5}$$

where $\boldsymbol{x}_k \in \mathbb{R}^6$, $\boldsymbol{z}_k \in \mathbb{R}^m$ and $\boldsymbol{\varepsilon}_k \in \mathbb{R}^m$ are the state, measurement, and measurement noise at the epoch t_k, respectively, $\boldsymbol{F} : \mathbb{R}^6 \mapsto \mathbb{R}^6$ represents the discrete dynamics equation, given by

$$\boldsymbol{F}(\boldsymbol{x}_{k-1}, t_{k-1}, t_k) = \int_{t_{k-1}}^{t_k} \boldsymbol{f}(\tau, \boldsymbol{x})d\tau + \boldsymbol{x}_{k-1}\,. \tag{6}$$

B. Extended Kalman filter

The extended Kalman filter (EKF) is a classic algorithm for solving OD problems and is taken as the base algorithm in this work. The EKF linearizes the nonlinear dynamics and measurement equations and then obtains the optimal estimation in a Bayesian filtering framework. The process of an EKF, following [35, 36], begins with the time update procedure.

The time update procedure calculates the predicted state and the associated a priori covariance. Given the estimated state $\hat{\boldsymbol{x}}_{k-1} \in \mathbb{R}^6$ and the associated covariance matrix $\hat{\boldsymbol{P}}_{k-1} \in \mathbb{R}^{6\times 6}$ at epoch t_{k-1}, the predicted state $\hat{\boldsymbol{x}}_{k|k-1} \in \mathbb{R}^6$ and the a priori covariance $\hat{\boldsymbol{P}}_{k|k-1} \in \mathbb{R}^{6\times 6}$ can be obtained as

$$\hat{\boldsymbol{x}}_{k|k-1} = \boldsymbol{F}(\hat{\boldsymbol{x}}_{k-1}, t_{k-1}, t_k) \,. \tag{7}$$

$$\hat{\boldsymbol{P}}_{k|k-1} = \boldsymbol{\Phi}_{t_{k-1}}^{t_k}(\hat{\boldsymbol{x}}_{k-1})\hat{\boldsymbol{P}}_{k-1}[\boldsymbol{\Phi}_{t_{k-1}}^{t_k}(\hat{\boldsymbol{x}}_{k-1})]^T + \boldsymbol{Q}_k \,, \tag{8}$$

where $\boldsymbol{Q}_k \in \mathbb{R}^{6\times 6}$ is the covariance matrix of the process noises at the epoch t_k and $\boldsymbol{\Phi}_{t_{k-1}}^{t_k}(\hat{\boldsymbol{x}}_{k-1}) = \frac{\partial \boldsymbol{F}(\hat{\boldsymbol{x}}_{k-1}, t_{k-1}, t_k)}{\partial \hat{\boldsymbol{x}}_{k-1}} \in \mathbb{R}^{6\times 6}$ is the state transition matrix (STM). The STM can be obtained by integrating Eq. (9) based on the estimated state $\hat{\boldsymbol{x}}_{k-1}$:

$$\begin{cases} \dot{\boldsymbol{\Phi}}_{t_{k-1}}^{\tau}(\hat{\boldsymbol{x}}_\tau) = \frac{\partial f(t, \hat{\boldsymbol{x}}_\tau)}{\partial \hat{\boldsymbol{x}}_\tau} \boldsymbol{\Phi}_{t_{k-1}}^{\tau}(\hat{\boldsymbol{x}}_\tau) \\ \boldsymbol{\Phi}_{t_{k-1}}^{t_{k-1}}(\hat{\boldsymbol{x}}_{k-1}) = \boldsymbol{I}_{6\times 6} \end{cases} . \tag{9}$$

Following the time update procedure is a measurement update procedure, which first calculates the predicted measurement $\hat{z}_{k|k-1} \in \mathbb{R}^m$, the cross-correlation covariance matrix $\hat{\boldsymbol{P}}_{k|k-1}^{\boldsymbol{xz}} \in \mathbb{R}^{6\times m}$, and the predicted measurement covariance matrix $\hat{\boldsymbol{P}}_{k|k-1}^{\boldsymbol{zz}} \in \mathbb{R}^{m\times m}$, given by

$$\hat{z}_{k|k-1} = \boldsymbol{h}(\hat{\boldsymbol{x}}_{k|k-1}) \,, \tag{10}$$

$$\hat{\boldsymbol{P}}_{k|k-1}^{\boldsymbol{xz}} = \hat{\boldsymbol{P}}_{k|k-1}\boldsymbol{H}_k^T \,, \tag{11}$$

$$\hat{\boldsymbol{P}}_{k|k-1}^{\boldsymbol{zz}} = \boldsymbol{H}_k\hat{\boldsymbol{P}}_{k|k-1}\boldsymbol{H}_k^T + \boldsymbol{R}_k \,, \tag{12}$$

where $\boldsymbol{R}_k = \{\boldsymbol{\varepsilon}_k\boldsymbol{\varepsilon}_k^T\} \in \mathbb{R}^{m\times m}$ is the covariance matrix of the measurement noise at epoch t_k, $\boldsymbol{H}_k = \frac{\partial \boldsymbol{h}(\hat{\boldsymbol{x}}_{k|k-1})}{\partial \hat{\boldsymbol{x}}_{k|k-1}} \in \mathbb{R}^{m\times 6}$ is the partial derivative matrix of the predicted measurement at epoch t_k with respect to the predicted state $\hat{\boldsymbol{x}}_{k|k-1}$.

On the receipt of the measurement z_k, the estimated state $\hat{\boldsymbol{x}}_k \in \mathbb{R}^6$ and the posterior (updated) covariance matrix $\hat{\boldsymbol{P}}_k \in \mathbb{R}^{6\times 6}$ at epoch t_k are obtained from

$$\boldsymbol{K}_k = \hat{\boldsymbol{P}}_{k|k-1}^{\boldsymbol{xz}}(\hat{\boldsymbol{P}}_{k|k-1}^{\boldsymbol{zz}})^{-1} \,, \tag{13}$$

$$\hat{\boldsymbol{x}}_k = \hat{\boldsymbol{x}}_{k|k-1} + \boldsymbol{K}_k(z_k - \hat{z}_{k|k-1}) \,, \tag{14}$$

$$\hat{\boldsymbol{P}}_k = \hat{\boldsymbol{P}}_{k|k-1} - \boldsymbol{K}_k \hat{\boldsymbol{P}}^{zz}_{k|k-1} \boldsymbol{K}_k^T . \tag{15}$$

C. Pixel area calculation using subpixel edge detection

Following [37], a subpixel edge detection algorithm is used to calculate the pixel area of the target asteroid in the image. The algorithm is composed of several steps, outlined in Fig. 1. The first step converts the input image (the raw image) to grayscale format, and then converts this grayscale image to binary image by thresholding. Thresholding is particularly useful when working with grayscale images as it simplifies the image and reduces noise. Letting I_{gray} ($0 \le I_{\text{gray}} \le 255$) and I_1 be the grayscale and binary images, respectively, then, the thresholding process is given as

$$I_1(i_x, i_y) = \begin{cases} 1 & I_{\text{gray}}(i_x, i_y) > \eta \\ 0 & \text{elsewise} \end{cases} , \tag{16}$$

where η is a user-defined threshold.

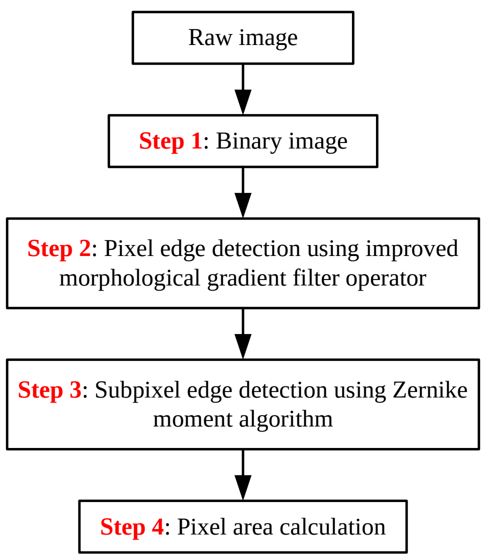

Fig. 1 Flowchart of the pixel area calculation algorithm.

In the second step, the Zernike moment algorithm is employed to realize the subpixel edge detection based on the pixel edge detection results from step 2; Zernike masks of size 7×7 are employed for subpixel edge detection. The process of the Zernike moment algorithm is detailed in Ref. [38]. Upon the subpixels of the asteroid edge detected by the Zernike moment algorithm, a polygon specified by these subpixels is constructed. Thereafter, the area of the polygon can be calculated, representing the asteroid's area on the image.

It should be noted that there are also some methods, such as the polynomial fitting algorithm, the ellipse fitting algorithm, the Gauss surface fitting algorithm, and the sigmoid curve fitting algorithm, that are available for subpixel edge detection and area calculation [37, 39]. The algorithm shown in Fig. 1 can be interchanged with other methods. The focus of this paper is improvement of optical-only OD performance by generating range measurement from the pixel area information, rather than the subpixel edge detection method or the pixel area calculation method.

III. Methodology

A. Vision-based range measurement model

Using the method presented in Sec. II.C, the pixel areas of the target asteroid at different epochs can be calculated. Let S_k and $S_{k-\delta}$ be the pixel areas of the target asteroid at a current epoch t_k and a prior epoch $t_{k-\delta}$, respectively, where $\delta \in \mathbb{N}^+$ and $t_{k-\delta}$ is an epoch prior to t_k. Then, a pixel area ratio can be obtained as

$$\kappa_k^{k-\delta} = \frac{S_k}{S_{k-\delta}}\,, \tag{17}$$

where $\kappa_{k-\delta}^{k}$ represents the ratio between the pixel areas at the epochs t_k and $t_{k-\delta}$. As shown in Fig. 2, $\Delta OAB \sim \Delta OA'B'$, which shows that the radius of the asteroid's projection on the image (AB) is inversely proportional to the range between the asteroid and the spacecraft OB' (say, $OB' \cdot AB = A'B' \cdot OB$). Note that the area is proportional to the square of the radius ($S_k \sim AB^2$), indicating that the area is inversely proportional to the square of the range. Therefore, a range ratio can be expressed as

$$\vartheta_k^{k-\delta} = \frac{\rho_k}{\rho_{k-\delta}} = \sqrt{\frac{1}{\kappa_k^{k-\delta}}} = \sqrt{\frac{S_{k-\delta}}{S_k}}\,, \tag{18}$$

where ρ_k and $\rho_{k-\delta}$ represent the ranges at the epochs t_k and $t_{k-\delta}$, respectively, $\vartheta_k^{k-\delta}$ stands for the range ratio of the epochs $t_{k-\delta}$ and t_k. Given the estimated state $\hat{\boldsymbol{x}}_k$ at current epoch t_k, a state at the prior epoch $t_{k-\delta}$, $\hat{\boldsymbol{x}}_{k-\delta|k} = [\hat{\boldsymbol{r}}_{k-\delta|k}; \hat{\boldsymbol{v}}_{k-\delta|k}]^T$, can be computed using Eq. (5) as

$$\hat{\boldsymbol{x}}_{k-\delta|k} = \boldsymbol{F}(\hat{\boldsymbol{x}}_k, t_k, t_{k-\delta}) \tag{19}$$

It should be noted that $\hat{\boldsymbol{x}}_{k-\delta|k} \neq \hat{\boldsymbol{x}}_{k-\delta}$ as $\hat{\boldsymbol{x}}_{k-\delta}$ represents the state estimated by the OD algorithm, whereas $\hat{\boldsymbol{x}}_{k-\delta|k}$ is a state propagated from epoch t_k to epoch $t_{k-\delta}$ based on $\hat{\boldsymbol{x}}_k$.

Combing Eq. (18) and Eq. (19)), a VBR measurement at epoch t_k can be obtained as

$$z_2(\boldsymbol{x}_k; \hat{\boldsymbol{x}}_k, \delta) = \vartheta_k^{k-\delta} \hat{\rho}_{k-\delta|k}\,, \tag{20}$$

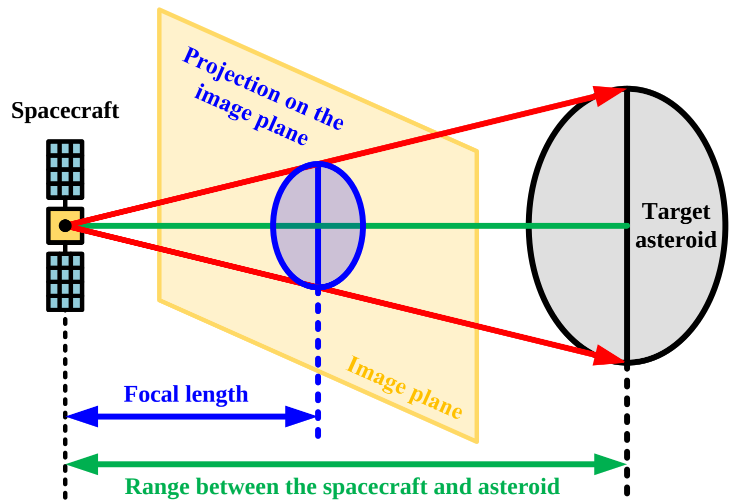

Fig. 2 An illustration of the relationship between the pixel area and the range.

where $\hat{\rho}_{k-\delta|k}$ is an estimated distance at the epoch $t_{k-\delta}$, which is computed based on the state $\hat{\boldsymbol{x}}_{k-\delta|k}$ as

$$\hat{\rho}_{k-\delta|k} = \left\| \hat{\boldsymbol{r}}_{k-\delta|k} - \boldsymbol{r}_a(t_{k-\delta}) \right\| , \tag{21}$$

Note that there are various variables that are related to the range between the asteroid and spacecraft. Table 1 is provided to distinguish these range variables and improve readability. One can see from Table 1 that, if $\delta = 0$, $\hat{\rho}_{k-\delta|k} = \hat{\rho}_k$. In addition, it should be noted that different from a regular measurement (*e.g.*, an angle measurement) that can be directly obtained from a sensor, the VBR measurement proposed in this paper is a combination of range ratio (can be directly obtained from optical sensors) and estimated state (*i.e.*, $\hat{\boldsymbol{x}}_k$, see Eq. (19)-(21)). However, it adds an additional, range-related constraint on the estimated state, that is, $\vartheta_k^{k-\delta}\hat{\rho}_{k-\delta|k} \approx \hat{\rho}_k$ (not an equal sign here due to the measurement noises). That constraint is independent of the angle measurement, which is expected to improve the OD accuracy.

B. Range ratio data preprocessing and covariance analysis

The shape of an asteroid can be modeled as a sphere (or an ellipsoid), and thus, the range ratio $\vartheta_k^{k-\delta}$ can be well-expressed using the pixel areas of the target asteroid (*i.e.*, S_k and $S_{k-\delta}$). However, due to the irregular shape and spin of many asteroids, including the asteroid considered in this work, the pixel areas of the target asteroid in the image are not only related to the range between the spacecraft and the asteroid, but also depend on the shape and spin state of the asteroid. In this case, the obtained VBR measurement has compound errors, and its uncertainties cannot be accurately modeled. A method is proposed herein to improve the accuracy of the VBR measurement for non-spherical

Table 1 Definitions of several range variables

Symbol	Definition	Expression	Additional statement
ρ_k	The true range at the given epoch t_k	$\rho_k = \|\boldsymbol{r}(t_k) - \boldsymbol{r}_a(t_k)\|$	
$\hat{\rho}_k$	An estimated range at the given epoch t_k	$\hat{\rho}_k = \|\hat{\boldsymbol{r}}(t_k) - \boldsymbol{r}_a(t_k)\|$	The position vector $\hat{\boldsymbol{r}}(t_k)$ is estimated by the filter.
$\hat{\rho}_{k-\delta\|k}$	An estimated range at a previous epoch $t_{k-\delta}$	$\hat{\rho}_{k-\delta\|k} = \left\|\hat{\boldsymbol{r}}_{k-\delta\|k} - \boldsymbol{r}_a(t_{k-\delta})\right\|$	The position vector $\hat{\boldsymbol{r}}_{k-\delta\|k}$ is obtained by propagating the estimated state $\hat{\boldsymbol{x}}_k$ from a epoch t_k back to a epoch $t_{k-\delta}$.
$z_2(\boldsymbol{x}_k; \hat{\boldsymbol{x}}_k, \delta)$	A VBR measurement at the given epoch t_k	$z_2(\boldsymbol{x}_k; \hat{\boldsymbol{x}}_k, \delta) = \vartheta_k^{k-\delta}\hat{\rho}_{k-\delta\|k}$	Various VBR measurements can be obtained at the given epoch t_k by changing the value for δ.

asteroids.

Assume that the images of the target asteroid are available at k+1 epochs $(t_0, t_1, \cdots, t_k)$. Then, a total of $\frac{k(k+1)}{2}$ range ratios can be obtained, given by

$$\begin{aligned}\mathcal{P}_k &= \left\{\vartheta_p^{q-\delta}\middle|\, \delta \le q \le p \le k, p \in \mathbb{N}^+, q \in \mathbb{N}^+, \delta \in \mathbb{N}^+\right\} \\ &= \begin{cases} \vartheta_k^{k-\delta_1} & \vartheta_k^{k-\delta_2} & \cdots & \vartheta_k^{k-\delta_{k-1}} & \vartheta_k^{k-\delta_k} \\ \vartheta_{k-1}^{k-1-\delta_1} & \vartheta_{k-1}^{k-1-\delta_2} & \cdots & \vartheta_{k-1}^{k-1-\delta_{k-1}} & \\ \vdots & \vdots & \iddots & & \\ \vartheta_2^{2-\delta_1} & \vartheta_2^{2-\delta_2} & & & \\ \vartheta_1^{1-\delta_1} & & & & \end{cases}\end{aligned}, \tag{22}$$

where $\mathcal{P}_k$ represents the set of range ratios available at epoch t_k and $\delta_j = j$ ($1 \le j \le k$ and $j \in \mathbb{N}^+$). With a given δ_j, k+1-j range ratios are available, which form the data set

$$\begin{aligned}\mathcal{P}_k(\delta_j) &= \left\{\vartheta_p^{q-\delta_j}\middle|\, \delta_j \le q \le p \le k, p \in \mathbb{N}^+, q \in \mathbb{N}^+\right\} \\ &= \left\{\vartheta_k^{k-\delta_j}, \vartheta_{k-1}^{k-1-\delta_j}, \cdots, \vartheta_{\delta_j}^{0}\right\}\end{aligned}, \tag{23}$$

where $\mathcal{P}_k(\delta_j) \subseteq \mathcal{P}_k$ is a collection of range ratios satisfying $\delta = \delta_j$.

To smooth the range ratio $\vartheta_k^{k-\delta_j}$, M successive elements, $\vartheta_k^{k-\delta_j}, \vartheta_{k-1}^{k-1-\delta_j}, \cdots, \vartheta_{k-M+1}^{k-\delta_j-M+1}$, are selected from the set $\mathcal{P}_k(\delta_j)$, where M is a user-defined parameters satisfying $M \le k+1-j$. Let ρ_i ($i \in \left\{k, k-1, \cdots, k-\delta_j-M+1\right\}$) and $\dot{\rho}_i$ be the true range and range rate at the epoch t_i. During the interval $[t_{k-\delta_j-M+1}, t_k]$, the range rate is approximated using a linear model as

$$\dot{\rho} \approx \dot{\rho}_{k-\delta_j-M+1} + \bar{\ddot{\rho}}(t - t_{k-\delta_j-M+1}), \tag{24}$$

where $\bar{\ddot{\rho}}$ denotes the averaged velocity rate in the given interval $[t_{k-\delta_j-M+1}, t_k]$. Here, the averaged velocity rate $\bar{\ddot{\rho}}$ is introduced to aid in deriving an approximated solution to smooth the range ratio measurements, and it will not be employed when implementing the algorithm. Using Eq. (24), the range between the spacecraft and the asteroid can be approximated using a quadratic expression as

$$\rho \approx \rho_{k-\delta_j-M+1} + \dot{\rho}_{k-\delta_j-M+1}(t - t_{k-\delta_j-M+1}) + \frac{\bar{\ddot{\rho}}(t - t_{k-\delta_j-M+1})^2}{2} \,. \tag{25}$$

Thus, the range ratio $\vartheta_i^{i-\delta_j}$ ($i \in \left\{k, k-1, \cdots, k-\delta_j-M+1\right\}$) can be approximated as

$$\begin{aligned}\vartheta_i^{i-\delta_j} &\approx \frac{\rho_{k-\delta_j-M+1} + \dot{\rho}_{k-\delta_j-M+1}\Delta\tau_i + \frac{\bar{\ddot{\rho}}(\Delta\tau_i)^2}{2}}{\rho_{k-\delta_j-M+1} + \dot{\rho}_{k-\delta_j-M+1}\Delta\tau_{i-\delta_j} + \frac{\bar{\ddot{\rho}}(\Delta\tau_{i-\delta_j})^2}{2}} \\ &= 1 + \frac{\dot{\rho}_{k-\delta_j-M+1}(\Delta\tau_i - \Delta\tau_{i-\delta_j}) + \bar{\ddot{\rho}}\frac{(\Delta\tau_i)^2-(\Delta\tau_{i-\delta_j})^2}{2}}{\rho_{k-\delta_j-M+1} + \dot{\rho}_{k-\delta_j-M+1}\Delta\tau_{i-\delta_j} + \frac{\bar{\ddot{\rho}}(\Delta\tau_{i-\delta_j})^2}{2}}\end{aligned} \,, \tag{26}$$

where $\Delta\tau_i = t_i - t_{k-\delta_j-M+1}$ and $\Delta\tau_{i-\delta_j} = t_{i-\delta_j} - t_{k-\delta_j-M+1}$ are introduced to simplify the expressions. Then, assuming that the length of the interval $[t_{k-\delta_j-M+1}, t_k]$ is much smaller than that of the approach phase, which holds if we select a small value of M, the change in the range is much smaller than the range itself. Thus,

$$\rho_{k-\delta_j-M+1} + \dot{\rho}_{k-\delta_j-M+1}\Delta\tau_{i-\delta_j} + \frac{\bar{\ddot{\rho}}(\Delta\tau_{i-\delta_j})^2}{2} \approx \rho_{k-\delta_j-M+1} \,, \tag{27}$$

$$(\Delta\tau_i)^2 - (\Delta\tau_{i-\delta_j})^2 = (\Delta\tau_i + \Delta\tau_{i-\delta_j})(\Delta\tau_i - \Delta\tau_{i-\delta_j}) \approx 2\Delta\tau_i(\Delta\tau_i - \Delta\tau_{i-\delta_j}) \,. \tag{28}$$

Substitution of Eqs. (27)-(28) into Eq. (26) gives

$$\vartheta_i^{i-\delta_j} \approx 1 + (\Delta\tau_i - \Delta\tau_{i-\delta_j})\frac{\dot{\rho}_{k-\delta_j-M+1} + \bar{\ddot{\rho}}\Delta\tau_i}{\rho_{k-\delta_j-M+1}} \,. \tag{29}$$

Let $c_0 = \frac{\dot{\rho}_{k-\delta_j-M+1}}{\rho_{k-\delta_j-M+1}}$ and $c_1 = \frac{\bar{\ddot{\rho}}}{\rho_{k-\delta_j-M+1}}$; then, Eq. (29) can be further written as

$$\vartheta_i^{i-\delta_j} \approx 1 + (\Delta\tau_i - \Delta\tau_{i-\delta_j})(c_0 + c_1\Delta\tau_i) \,, \tag{30}$$

where c_0 and c_1 are two coefficients to be fitted using the selected M range ratios. Recall that the algorithm doesn't require an exact value or an initial guess for the averaged velocity rate $\bar{\ddot{\rho}}$; instead, it indirectly estimates $\bar{\ddot{\rho}}$ by determining the coefficient c_1, and thereby, smoothing the incoming range ratio data. Let $\hat{\vartheta}_i^{i-\delta_j} = 1 + c_0\tau_{i-\delta_j}^i + c_1\tau_{i-\delta_j}^i\tau_{k-\delta_j-M+1}^i$

be the predicted range ratio at the epoch t_i. Then, the residual error at the epoch t_i can be formed as

$$e_i = \hat{\vartheta}_i^{i-\delta_j} - \vartheta_i^{i-\delta_j} = 1 + (\Delta\tau_i - \Delta\tau_{i-\delta_j})(c_0 + c_1\Delta\tau_i) - \vartheta_i^{i-\delta_j} . \tag{31}$$

The coefficients c_0 and c_1 in Eq. (30) can be determined by minimizing the sum of the absolute values of residual errors in Eq. (31). The cost function is written as

$$J = \sum_{i=k+1-M}^{k} |e_i| . \tag{32}$$

Note that the distance between the spacecraft and the asteroid usually becomes smaller as the spacecraft moves closer to the asteroid. Therefore, a constraint is added as

$$\hat{\vartheta}_i^{i-\delta_j} - 1 = (\Delta\tau_i - \Delta\tau_{i-\delta_j})(c_0 + c_1\Delta\tau_i) \leq 0 . \tag{33}$$

The constraint in Eq. (33) is employed for the approaching phase. If the spacecraft is departing the asteroid, the constraint can be rewritten as $\hat{\vartheta}_i^{i-\delta_j} - 1 = (\Delta\tau_i - \Delta\tau_{i-\delta_j})(c_0 + c_1\Delta\tau_i) \geq 0$. However, if an additional maneuver is executed, the assumption of being closer to the asteroid is not valid, which is one of the limitations of this smoothing method.

Noting that $\Delta\tau_i - \Delta\tau_{i-\delta_j} = (t_i - t_{k-\delta_j-M+1}) - (t_{i-\delta_j} - t_{k-\delta_j-M+1}) = t_i - t_{i-\delta_j} > 0$. Then, using Eqs. (32)-(33), an optimization problem is defined as

$$\begin{aligned} \min_{c_0,c_1} \quad & J = \sum_{i=k+1-M}^{k} |e_i| \\ s.t. \quad & c_0 + c_1\Delta\tau_i \leq 0 \end{aligned} . \tag{34}$$

The optimization problem in Eq. (34) is difficult to solve as it is non-convex. To address the optimization problem and make it easier to determine the coefficients, define a slack variable $\boldsymbol{s} = [s_{k+1-M}, \cdots, s_k]^T \in \mathbb{R}^M$, which satisfies

$$|e_i| \leq s_i ; \text{for}\, i = k + 1 - M, \cdots, k , \tag{35}$$

The inequation in Eq. (35) can be further rewritten as

$$\begin{aligned} 1 + (\Delta\tau_i - \Delta\tau_{i-\delta_j})(c_0 + c_1\Delta\tau_i) - \vartheta_i^{i-\delta_j} &\leq s_i \\ 1 + (\Delta\tau_i - \Delta\tau_{i-\delta_j})(c_0 + c_1\Delta\tau_i) - \vartheta_i^{i-\delta_j} &\geq -s_i \end{aligned} . \tag{36}$$

Rearrange the terms in Eqs. (33) and (36) and define $\boldsymbol{\chi} = [c_1; c_0; \boldsymbol{s}] \in \mathbb{R}^{M+2}$; then, the constraints in Eqs. (33) and (36) can be rewritten in the matrix form

$$\boldsymbol{A}\boldsymbol{\chi} \leq \boldsymbol{B} , \tag{37}$$

where

$$\boldsymbol{A} = \begin{bmatrix} [\boldsymbol{A}_1, \boldsymbol{A}_1] \odot \boldsymbol{A}_2 & -\boldsymbol{I}_M \\ -[\boldsymbol{A}_1, \boldsymbol{A}_1] \odot \boldsymbol{A}_2 & -\boldsymbol{I}_M \\ \boldsymbol{A}_2 & \boldsymbol{0}_{M\times M} \end{bmatrix} \in \mathbb{R}^{3M\times(M+2)}, \tag{38}$$

$$\boldsymbol{A}_1 = \begin{bmatrix} \Delta\tau_{k+1-M} - \Delta\tau_{k-\delta_j} \\ \vdots \\ \Delta\tau_k - \Delta\tau_{k-\delta_j} \end{bmatrix} \in \mathbb{R}^{(M+1)}, \boldsymbol{A}_2 = \begin{bmatrix} 1 & \Delta\tau_{k+1-M} \\ \vdots & \vdots \\ 1 & \Delta\tau_k \end{bmatrix} \in \mathbb{R}^{(M+1)\times 2} \tag{39}$$

$$\boldsymbol{B} = \begin{bmatrix} \boldsymbol{B}_1 \\ -\boldsymbol{B}_1 \\ \boldsymbol{0}_{M\times 1} \end{bmatrix} \in {}^{3M\times 1}, \boldsymbol{B}_1 = \left[\vartheta_{k+1-M}^{k+1-M-\delta_j}, \cdots, \vartheta_k^{k-\delta_j}\right]^T \in \mathbb{R}^{M\times 1}. \tag{40}$$

In Eqs. (38)-(40), $\odot$ is an element-wise multiplication operator, and $\boldsymbol{0}_{p\times q} = [0]_{p\times q}$ and $\boldsymbol{I}_{p\times q} = [1]_{p\times q}$ are matrixes of size $p \times q$ ($p, q \in \mathbb{N}^+$) with elements being 0 and 1, respectively.

Using the vector $\boldsymbol{\chi}$, the cost function given in Eq. (34) is rewritten, and the non-convex optimization problem is further formulated as a linear programming problem (LPP) as

$$\begin{aligned} \min_{\chi} \quad & J = \boldsymbol{c}^T \chi \\ \text{s.t.} \quad & \boldsymbol{A}\chi \leq \boldsymbol{B} \end{aligned}, \tag{41}$$

where $\boldsymbol{c} = [\boldsymbol{0}_{1\times 2}, \boldsymbol{I}_{1\times M}]^T \in \mathbb{R}^{(M+2)\times 1}$. In this paper, the LPP in Eq. (41) is solved using an interior-point optimizer MOSEK*. Once the LPP is solved, the predicted (smoothed) range ratio at the epoch t_k, $\hat{\vartheta}_k^{k-\delta_j}$, is obtained using Eq. (30).

A further difficulty in using the VBR measurement for asteroid approach OD lies in how to model the uncertainty (usually represented by the standard deviation [STD]) of the measurement. Without modeling the measurement uncertainties and constructing the measurement noise matrix (as shown in Eq. (12)), the filter algorithm cannot update the estimated state and obtain the posterior covariance matrix. In this work, the STD of the predicted error of range ratio $\hat{\vartheta}_k^{k-\delta_j}$ is approximated by the STD of the residual error e_i, given as

$$\sigma(\hat{\vartheta}_k^{k-\delta_j}) \approx \sigma(e_i) = \sqrt{\frac{\sum_{k+1-M}^{k}\left(e_i - \frac{\sum_{k+1-M}^{k} e_i}{M}\right)^2}{M}}. \tag{42}$$

*Available at `https://www.mosek.com/` [retrieved on January 2025]

The covariance of the range ratio error is then expressed as

$$P_k^{k-\delta_j} = \mathbb{E}\{(\Delta\vartheta_k^{k-\delta_j})^2\} \approx \left[\sigma(\hat{\vartheta}_k^{k-\delta_j})\right]^2, \tag{43}$$

where $\Delta\vartheta_k^{k-\delta_j} = \hat{\vartheta}_k^{k-\delta_j} - \frac{\rho_k}{\rho_{k-\delta_j}}$ represents the true range ratio error. Substitution of the expression of $\Delta\vartheta_k^{k-\delta_j}$ into Eq. (20) yields

$$\begin{aligned} z_2(\boldsymbol{x}_k;\hat{\boldsymbol{x}}_k,\delta_j) &= \vartheta_k^{k-\delta_j}\hat{\rho}_{k-\delta_j|k} \approx \hat{\vartheta}_k^{k-\delta_j}\hat{\rho}_{k-\delta_j|k} \\ &= \left(\frac{\rho_k}{\rho_{k-\delta_j}} - \Delta\vartheta_k^{k-\delta_j}\right)\hat{\rho}_{k-\delta_j|k} = \frac{\rho_k}{\rho_{k-\delta_j}}\hat{\rho}_{k-\delta_j|k} - \Delta\vartheta_k^{k-\delta_j}\hat{\rho}_{k-\delta_j|k} \end{aligned}, \tag{44}$$

where $z_2(\boldsymbol{x}_k;\hat{\boldsymbol{x}}_k,\delta_j) \in \mathbb{R}^1$ represents the VBR with a given δ_j at the epoch t_k. Considering more than one VBR measurement, the model given in Eq. (44) can be further written as

$$z_2(\boldsymbol{x}_k;\hat{\boldsymbol{x}}_k,\delta_{j_1},\delta_{j_2},\cdots,\delta_{j_{n_{\mathrm{VBR}}}}) = \begin{bmatrix} \frac{\rho_k}{\rho_{k-\delta_{j_1}}}\hat{\rho}_{k-\delta_{j_1}|k} + \Delta\vartheta_k^{k-\delta_{j_1}}\hat{\rho}_{k-\delta_{j_1}|k} \\ \frac{\rho_k}{\rho_{k-\delta_{j_2}}}\hat{\rho}_{k-\delta_{j_2}|k} + \Delta\vartheta_k^{k-\delta_{j_2}}\hat{\rho}_{k-\delta_{j_2}|k} \\ \vdots \\ \frac{\rho_k}{\rho_{k-\delta_{j_{n_{\mathrm{VBR}}}}}}\hat{\rho}_{k-\delta_{j_{n_{\mathrm{VBR}}}}|k} + \Delta\vartheta_k^{k-\delta_{j_{n_{\mathrm{VBR}}}}}\hat{\rho}_{k-\delta_{j_{n_{\mathrm{VBR}}}}|k} \end{bmatrix}, \tag{45}$$

where $z_2(\boldsymbol{x}_k;\hat{\boldsymbol{x}}_k,\delta_{j_1},\delta_{j_2},\cdots,\delta_{j_{n_{VBR}}}) \in \mathbb{R}^{n_{\mathrm{VBR}}}$ and n_{VBR} is the number of VBR measurements per epoch. It should be noted that Eqs. (44)-(45) don't mean that the VBR measurement relies on the true range (*i.e.*, ρ_k and $\rho_{k-\delta_j}$). Instead, by splitting the range ratio data $\hat{\vartheta}_k^{k-\delta}$ into a true part $\frac{\rho_k}{\rho_{k-\delta_j}}$ and a noise part $\Delta\vartheta_k^{k-\delta_j}$, we can easily investigate the OD system uncertainties and derive the expression for the covariance matrixes, which will be shown in the next subsection.

According to the above discussion, the process of generating a VBR measurement is detailed in Table 2. Multiple VBR measurements can be obtained by changing the value for δ_j. It can provide more information related to the orbit, which can be considered as a constraint on the ranges at both epochs t_k and $t_{k-\delta_j}$. Thus, if n_{VBR} increases, the estimation is expected to be more accurate as more constraints are added.

C. System modeling with VBR measurements

For a filter algorithm (say, EKF), comparisons between the collected measurements and the predicted measurements are required. The differences between the collected measurements and the predicted measurements are usually called measurement residuals. The uncertainty of the measurement residuals is described using the predicted measurement covariance matrix $\hat{\boldsymbol{P}}_{k|k-1}^{\boldsymbol{zz}}$ (as shown in Eq. (12)). In a standard case, the measurement at a given epoch, t_k, only depends on the state at that epoch, t_k. However, the VBR measurement model contains both the current state and the previous

Table 2 Procedure to generate a VBR measurement

procedure $[z_2(\boldsymbol{x}_k;\hat{\boldsymbol{x}}_k,\delta_j), P_k^{k-\delta_j}]$ = **generateVBR**($\hat{\boldsymbol{x}}_k, t_k, M, \delta_j$)
1: Compute the pixel areas at various epochs to obtain S_i ($i \in \mathbb{N}^+, i \le k$) ▷ Sec. II.C
2: Compute the range ratios to construct the data set $\mathcal{P}_k(\delta_j)$. ▷ Eq. (23)
3: Select M range ratios from the data set $\mathcal{P}_k(\delta_j)$ and smooth them to obtain $\hat{\vartheta}_k^{k-\delta_j}$. ▷ Eq. (41)
4: Propagate the estimated state $\hat{\boldsymbol{x}}_k$ from the t_k back to $t_{k-\delta_j}$ to obtain $\hat{\boldsymbol{r}}_{k-\delta_j\|k}$. ▷ Eq. (19)
5: Compute the estimated range $\hat{\rho}_{k-\delta_j\|k}$. ▷ Eq. (21)
6: Compute the VBR measurement as $z_2(\boldsymbol{x}_k;\hat{\boldsymbol{x}}_k,\delta_j) \approx \hat{\vartheta}_k^{k-\delta_j}\hat{\rho}_{k-\delta_j\|k}$ ▷ Eq. (20)
7: Compute the covariance matrix as $P_k^{k-\delta_j} \approx [\sigma(\hat{\vartheta}_k^{k-\delta_j})]^2$. ▷ Eqs. (42)-(43)
return $z_2(\boldsymbol{x}_k;\hat{\boldsymbol{x}}_k,\delta_j)$ and $P_k^{k-\delta_j}$

state, as range ratios rely on data at different epochs (as shown in Eqs. (44)-(45)). In this case, Eq. (12) no longer holds, requiring a new expression for $\hat{\boldsymbol{P}}^{zz}_{k|k-1}$. In general, the predicted measurement covariance matrix $\hat{\boldsymbol{P}}^{zz}_{k|k-1}$ is defined as

$$\hat{\boldsymbol{P}}^{zz}_{k|k-1} = \mathbb{E}\{(z_k - \mathbb{E}\{z_k\})(z_k - \mathbb{E}\{z_k\})^T\}\,. \tag{46}$$

Note that $\mathbb{E}\{z_k\} = \boldsymbol{h}(\hat{\boldsymbol{x}}_{k|k-1})$ since $\mathbb{E}\{\boldsymbol{\varepsilon}_k\} \in \boldsymbol{0}_{m\times 1}$.Then, the measurement covariance matrix $\hat{\boldsymbol{P}}^{zz}_{k|k-1}$ is rewritten as

$$\hat{\boldsymbol{P}}^{zz}_{k|k-1} = \mathbb{E}\{[z_k - \boldsymbol{h}(\hat{\boldsymbol{x}}_{k|k-1})][z_k - \boldsymbol{h}(\hat{\boldsymbol{x}}_{k|k-1})]^T\}\,. \tag{47}$$

Using Eq. (3), the measurement covariance matrix $\hat{\boldsymbol{P}}^{zz}_{k|k-1}$ can be partitioned as

$$\hat{\boldsymbol{P}}^{zz}_{k|k-1} = \begin{bmatrix} \hat{\boldsymbol{P}}^{zz}_{11,k|k-1} & \hat{\boldsymbol{P}}^{zz}_{12,k|k-1} \\ \hat{\boldsymbol{P}}^{zz}_{21,k|k-1} & \hat{\boldsymbol{P}}^{zz}_{22,k|k-1} \end{bmatrix}, \tag{48}$$

where

$$\hat{\boldsymbol{P}}^{zz}_{ij,k|k-1} = \mathbb{E}\{[z_{i,k} - \boldsymbol{h}_i(\hat{\boldsymbol{x}}_{k|k-1})][z_{j,k} - \boldsymbol{h}_j(\hat{\boldsymbol{x}}_{k|k-1})]^T\}\,. \tag{49}$$

Substituting the equation $z_{1,k} = \boldsymbol{h}_1(\boldsymbol{x}_k) + \boldsymbol{\varepsilon}_{1,k}$ into Eq. (49), multiplying out terms, and taking $\boldsymbol{\varepsilon}_{1,k}$ and $\boldsymbol{h}_1(\boldsymbol{x}_k)$ to be pairwise uncorrelated [40], $\hat{\boldsymbol{P}}^{zz}_{11,k|k-1}$ can be rewritten as

$$\begin{aligned} \hat{\boldsymbol{P}}^{zz}_{11,k|k-1} &= \mathbb{E}\{[\boldsymbol{h}_1(\boldsymbol{x}_k) + \boldsymbol{\varepsilon}_{1,k} - \boldsymbol{h}_1(\hat{\boldsymbol{x}}_{k|k-1})][\boldsymbol{h}_1(\boldsymbol{x}_k) + \boldsymbol{\varepsilon}_{1,k} - \boldsymbol{h}_1(\hat{\boldsymbol{x}}_{k|k-1})]^T\} \\ &= \mathbb{E}\{\boldsymbol{h}_1(\boldsymbol{x}_k)\boldsymbol{h}_1^T(\boldsymbol{x}_k)\} - \boldsymbol{h}_1(\hat{\boldsymbol{x}}_{k|k-1})\boldsymbol{h}_1^T(\hat{\boldsymbol{x}}_{k|k-1}) + \mathbb{E}\{\boldsymbol{\varepsilon}_{1,k}\boldsymbol{\varepsilon}_{1,k}^T\} \end{aligned}. \tag{50}$$

Let $\boldsymbol{R}_{1,k} = \mathbb{E}\{\boldsymbol{\varepsilon}_{1,k}\boldsymbol{\varepsilon}_{1,k}^T\} \in \mathbb{R}^{2\times 2}$ be the covariance matrix of the angle measurement. After defining $\delta\boldsymbol{x}_k = \boldsymbol{x}_k - \hat{\boldsymbol{x}}_{k|k-1}$

and expanding $\boldsymbol{h}_1(\boldsymbol{x}_k)$ in a Taylor series, with respect to $\hat{\boldsymbol{x}}_{k|k-1}$, yields the first-order approximation

$$\boldsymbol{h}_1(\boldsymbol{x}_k) = \boldsymbol{h}_1(\hat{\boldsymbol{x}}_{k|k-1} + \delta\boldsymbol{x}_k) \approx \boldsymbol{h}_1(\hat{\boldsymbol{x}}_{k|k-1}) + \boldsymbol{H}_{1,k}\delta\boldsymbol{x}_k \,, \tag{51}$$

where

$$\boldsymbol{H}_{1,k}(\hat{\boldsymbol{x}}_{k|k-1}) = \left.\frac{\partial \boldsymbol{h}_1(\boldsymbol{x})}{\partial \boldsymbol{x}}\right|_{\boldsymbol{x}=\hat{\boldsymbol{x}}_{k|k-1}} \overset{\text{abbr.}}{=} \boldsymbol{H}_{1,k} \,. \tag{52}$$

Using Eq. (51) and recalling that $\hat{\boldsymbol{P}}_{k|k-1} = \mathbb{E}\{\delta\boldsymbol{x}_k\delta\boldsymbol{x}_k^T\}$ and $\boldsymbol{R}_{1,k} = \mathbb{E}\{\boldsymbol{\varepsilon}_{1,k}\boldsymbol{\varepsilon}_{1,k}^T\}$,

$$\hat{\boldsymbol{P}}^{zz}_{11,k|k-1} \approx \boldsymbol{H}_{1,k}\hat{\boldsymbol{P}}_{k|k-1}\boldsymbol{H}_{1,k}^T + \boldsymbol{R}_{1,k} \,. \tag{53}$$

Then, the expression for $\hat{\boldsymbol{P}}^{zz}_{22,k|k-1}$ can be derived. First, consider the case of $n_{\text{VBR}} = 1$ (Eq. (44)). Substituting Eq. (44) into Eq. (49), $\hat{\boldsymbol{P}}^{zz}_{22,k|k-1}$ is rewritten as

$$\hat{\boldsymbol{P}}^{zz}_{22,k|k-1} = \mathbb{E}\left\{\left[\frac{\rho_k}{\rho_{k-\delta_j}}\hat{\rho}_{k-\delta_j|k} + \Delta\vartheta_k^{k-\delta_j}\hat{\rho}_{k-\delta_j|k} - \boldsymbol{h}_2(\hat{\boldsymbol{x}}_{k|k-1})\right]^2\right\} \,, \tag{54}$$

where

$$\frac{\rho_k}{\rho_{k-\delta_j}}\hat{\rho}_{k-\delta_j|k} - \boldsymbol{h}_2(\hat{\boldsymbol{x}}_{k|k-1}) = \frac{\boldsymbol{h}_2(\boldsymbol{x}_k)}{\boldsymbol{h}_2(\boldsymbol{x}_{k-\delta_j})}\boldsymbol{h}_2(\hat{\boldsymbol{x}}_{k-\delta_j|k}) - \boldsymbol{h}_2(\hat{\boldsymbol{x}}_{k|k-1}) \,. \tag{55}$$

Using the Taylor series expansion, $\boldsymbol{h}_2(\boldsymbol{x}_k)$ and $\boldsymbol{h}_2(\boldsymbol{x}_{k-\delta_j})$ can be approximated as

$$\boldsymbol{h}_2(\boldsymbol{x}_k) \approx \boldsymbol{h}_2(\hat{\boldsymbol{x}}_{k|k-1}) + \boldsymbol{H}_{2,k}\delta\boldsymbol{x}_k \,, \tag{56}$$

$$\boldsymbol{h}_2(\boldsymbol{x}_{k-\delta_j}) \approx \boldsymbol{h}_2(\hat{\boldsymbol{x}}_{k-\delta_j|k}) + \boldsymbol{H}_{2,k-\delta_j}\delta\boldsymbol{x}_{k-\delta_j} \,, \tag{57}$$

where $\delta\boldsymbol{x}_{k-\delta_j} = \boldsymbol{x}_{k-\delta_j} - \hat{\boldsymbol{x}}_{k-\delta_j|k}$ and

$$\boldsymbol{H}_{2,k}(\hat{\boldsymbol{x}}_{k|k-1}) = \left.\frac{\partial \boldsymbol{h}_2(\boldsymbol{x})}{\partial \boldsymbol{x}}\right|_{\boldsymbol{x}=\hat{\boldsymbol{x}}_{k|k-1}} \overset{\text{abbr.}}{=} \boldsymbol{H}_{2,k} \,, \tag{58}$$

$$\boldsymbol{H}_{2,k-\delta}(\hat{\boldsymbol{x}}_{k-\delta_j|k}) = \left.\frac{\partial \boldsymbol{h}_2(\boldsymbol{x})}{\partial \boldsymbol{x}}\right|_{\boldsymbol{x}=\hat{\boldsymbol{x}}_{k-\delta_j|k}} \overset{\text{abbr.}}{=} \boldsymbol{H}_{2,k-\delta_j} \,. \tag{59}$$

The two deviations, $\delta\boldsymbol{x}_{k-\delta_j}$ and $\delta\boldsymbol{x}_k$, can be connected using an STM as

$$\delta\boldsymbol{x}_{k-\delta_j} \approx \left[\boldsymbol{\Phi}^{t_k}_{t_{k-\delta_j}}(\hat{\boldsymbol{x}}_{k|k-1})\right]^{-1}\delta\boldsymbol{x}_k \,, \tag{60}$$

where $\boldsymbol{\Phi}^{t_k}_{t_{k-\delta_j}}(\hat{\boldsymbol{x}}_{k|k-1})$ stands for the STM from epoch $t_{k-\delta_j}$ to epoch t_k based on the state $\hat{\boldsymbol{x}}_{k|k-1}$. Using Eqs. (56)-(60)

yields

$$\frac{\boldsymbol{h}_2(\boldsymbol{x}_k)}{\boldsymbol{h}_2(\boldsymbol{x}_{k-\delta_j})} \approx \begin{array}{l} \dfrac{\boldsymbol{h}_2(\hat{\boldsymbol{x}}_k)}{\boldsymbol{h}_2(\hat{\boldsymbol{x}}_{k-\delta_j|k}) + \boldsymbol{H}_{2,k-\delta_j}\left[\boldsymbol{\Phi}_{t_{k-\delta_j}}^{t_k}(\hat{\boldsymbol{x}}_{k|k-1})\right]^{-1}\delta\boldsymbol{x}_k} \\ + \dfrac{\boldsymbol{H}_{2,k}\delta\boldsymbol{x}_k}{\boldsymbol{h}_2(\hat{\boldsymbol{x}}_{k-\delta_j|k}) + \boldsymbol{H}_{2,k-\delta_j}\left[\boldsymbol{\Phi}_{t_{k-\delta_j}}^{t_k}(\hat{\boldsymbol{x}}_{k|k-1})\right]^{-1}\delta\boldsymbol{x}_k} \end{array} . \tag{61}$$

Note that

$$\frac{\boldsymbol{h}_2(\hat{\boldsymbol{x}}_k)}{\boldsymbol{h}_2(\hat{\boldsymbol{x}}_{k-\delta_j|k}) + \boldsymbol{H}_{2,k-\delta_j}\left[\boldsymbol{\Phi}_{t_{k-\delta_j}}^{t_k}(\hat{\boldsymbol{x}}_{k|k-1})\right]^{-1}\delta\boldsymbol{x}_k} \approx \begin{array}{l} -\dfrac{\boldsymbol{h}_2(\hat{\boldsymbol{x}}_k)}{\left[\boldsymbol{h}_2(\hat{\boldsymbol{x}}_{k-\delta_j|k})\right]^2}\boldsymbol{H}_{2,k-\delta_j}\left[\boldsymbol{\Phi}_{t_{k-\delta_j}}^{t_k}(\hat{\boldsymbol{x}}_{k|k-1})\right]^{-1}\delta\boldsymbol{x}_k \\ + \dfrac{\boldsymbol{h}_2(\hat{\boldsymbol{x}}_k)}{\boldsymbol{h}_2(\hat{\boldsymbol{x}}_{k-\delta_j|k})} \end{array} , \tag{62}$$

$$\frac{\boldsymbol{H}_{2,k}\delta\boldsymbol{x}_k}{\boldsymbol{h}_2(\hat{\boldsymbol{x}}_{k-\delta_j|k}) + \boldsymbol{H}_{2,k-\delta_j}\left[\boldsymbol{\Phi}_{t_{k-\delta_j}}^{t_k}(\hat{\boldsymbol{x}}_{k|k-1})\right]^{-1}\delta\boldsymbol{x}_k} \approx \frac{\boldsymbol{H}_{2,k}\delta\boldsymbol{x}_k}{\boldsymbol{h}_2(\hat{\boldsymbol{x}}_{k-\delta_j|k})} . \tag{63}$$

Substituting Eqs. (61)-(63) into Eq. (55) yields

$$\begin{aligned} &\frac{\boldsymbol{h}_2(\boldsymbol{x}_k)}{\boldsymbol{h}_2(\boldsymbol{x}_{k-\delta_j})}\boldsymbol{h}_2(\hat{\boldsymbol{x}}_{k-\delta_j|k}) - \boldsymbol{h}_2(\hat{\boldsymbol{x}}_{k|k-1}) \\ &\approx \left\{\frac{\boldsymbol{H}_{2,k}\delta\boldsymbol{x}_k}{\boldsymbol{h}_2(\hat{\boldsymbol{x}}_{k-\delta_j|k})} + \frac{\boldsymbol{h}_2(\hat{\boldsymbol{x}}_k)}{\boldsymbol{h}_2(\hat{\boldsymbol{x}}_{k-\delta_j|k})} - \frac{\boldsymbol{h}_2(\hat{\boldsymbol{x}}_k)}{\left[\boldsymbol{h}_2(\hat{\boldsymbol{x}}_{k-\delta_j|k})\right]^2}\boldsymbol{H}_{2,k-\delta_j}\left[\boldsymbol{\Phi}_{t_{k-\delta_j}}^{t_k}(\hat{\boldsymbol{x}}_{k|k-1})\right]^{-1}\delta\boldsymbol{x}_k\right\}\boldsymbol{h}_2(\hat{\boldsymbol{x}}_{k-\delta_j|k}) - \boldsymbol{h}_2(\hat{\boldsymbol{x}}_k) . \\ &= \boldsymbol{H}_{2,k}\delta\boldsymbol{x}_k - \frac{\boldsymbol{h}_2(\hat{\boldsymbol{x}}_k)}{\boldsymbol{h}_2(\hat{\boldsymbol{x}}_{k-\delta_j|k})}\boldsymbol{H}_{2,k-\delta_j}\left[\boldsymbol{\Phi}_{t_{k-\delta_j}}^{t_k}(\hat{\boldsymbol{x}}_{k|k-1})\right]^{-1}\delta\boldsymbol{x}_k \end{aligned} \tag{64}$$

Substituting Eq. (64) into Eq. (54), $\hat{\boldsymbol{P}}_{22,k|k-1}^{zz}$ can be further expressed as

$$\begin{aligned} \hat{\boldsymbol{P}}_{22,k|k-1}^{zz} &\approx \left\{\left[\tilde{\boldsymbol{H}}_{2,k}\delta\boldsymbol{x}_k + \Delta\vartheta_k^{k-\delta_j}\hat{\rho}_{k-\delta_j|k}\right]^2\right\} = \tilde{\boldsymbol{H}}_{2,k}\hat{\boldsymbol{P}}_{k|k-1}\tilde{\boldsymbol{H}}_{2,k}^T + (\hat{\rho}_{k-\delta_j|k})^2\{\Delta\vartheta_k^{k-\delta_j}\Delta\vartheta_k^{k-\delta_j}\} \\ &= \tilde{\boldsymbol{H}}_{2,k}\hat{\boldsymbol{P}}_{k|k-1}\tilde{\boldsymbol{H}}_{2,k}^T + (\hat{\rho}_{k-\delta_j|k})^2 P_k^{k-\delta_j} \end{aligned} , \tag{65}$$

where

$$\tilde{\boldsymbol{H}}_{2,k} = \boldsymbol{H}_{2,k} - \frac{\boldsymbol{h}_2(\hat{\boldsymbol{x}}_k)}{\boldsymbol{h}_2(\hat{\boldsymbol{x}}_{k-\delta_j|k})}\boldsymbol{H}_{2,k-\delta_j}\left[\boldsymbol{\Phi}_{t_{k-\delta_j}}^{t_k}(\hat{\boldsymbol{x}}_{k|k-1})\right]^{-1} . \tag{66}$$

Similarly,

$$\hat{\boldsymbol{P}}_{12,k|k-1}^{zz} \approx \mathbb{E}\left\{\left[\boldsymbol{H}_{1,k}\delta\boldsymbol{x}_k + \boldsymbol{\varepsilon}_{1,k}\right] \times \left[\tilde{\boldsymbol{H}}_{2,k}\delta\boldsymbol{x}_k + \Delta\vartheta_k^{k-\delta_j}\hat{\rho}_{k-\delta_j|k}\right]\right\} = \boldsymbol{H}_{1,k}\hat{\boldsymbol{P}}_{k|k-1}\tilde{\boldsymbol{H}}_{2,k}^T , \tag{67}$$

$$\hat{\boldsymbol{P}}_{21,k|k-1}^{zz} \approx \mathbb{E}\left\{\left[\tilde{\boldsymbol{H}}_{2,k}\delta\boldsymbol{x}_k + \Delta\vartheta_k^{k-\delta_j}\hat{\rho}_{k-\delta_j|k}\right] \times \left[\boldsymbol{H}_{1,k}\delta\boldsymbol{x}_k + \boldsymbol{\varepsilon}_{1,k}\right]^T\right\} = \tilde{\boldsymbol{H}}_{2,k}\hat{\boldsymbol{P}}_{k|k-1}\boldsymbol{H}_{1,k}^T . \tag{68}$$

Substituting Eqs. (53), (65), (67) and (68) into Eq. (48), the measurement covariance matrix $\hat{\boldsymbol{P}}^{zz}_{k|k-1}$ is derived as

$$\hat{\boldsymbol{P}}^{zz}_{k|k-1} \approx \begin{bmatrix} \boldsymbol{H}_{1,k}\hat{\boldsymbol{P}}_{k|k-1}\boldsymbol{H}^T_{1,k} + \boldsymbol{R}_{1,k} & \boldsymbol{H}_{1,k}\hat{\boldsymbol{P}}_{k|k-1}\tilde{\boldsymbol{H}}^T_{2,k} \\ \tilde{\boldsymbol{H}}_{2,k}\hat{\boldsymbol{P}}_{k|k-1}\boldsymbol{H}^T_{1,k} & \tilde{\boldsymbol{H}}_{2,k}\hat{\boldsymbol{P}}_{k|k-1}\tilde{\boldsymbol{H}}^T_{2,k} + (\hat{\rho}_{k-\delta_j|k})^2 P^{k-\delta_j}_k \end{bmatrix} . \tag{69}$$

Let $\tilde{\boldsymbol{H}}_k = [\boldsymbol{H}_{1,k}; \tilde{\boldsymbol{H}}_{2,k}] \in \mathbb{R}^{3\times6}$ and $\tilde{\boldsymbol{R}}_k = \begin{bmatrix} \boldsymbol{R}_{1,k} & \mathbf{0}_{2\times1} \\ \mathbf{0}_{1\times2} & (\hat{\rho}_{k-\delta_j|k})^2 P^{k-\delta_j}_k \end{bmatrix} \in \mathbb{R}^{3\times3}$; then Eq. (69) can be further expressed as

$$\hat{\boldsymbol{P}}^{zz}_{k|k-1} \approx \tilde{\boldsymbol{H}}_k\hat{\boldsymbol{P}}_{k|k-1}\tilde{\boldsymbol{H}}^T_k + \tilde{\boldsymbol{R}}_k . \tag{70}$$

The two terms $\tilde{\boldsymbol{H}}_k\hat{\boldsymbol{P}}_{k|k-1}\tilde{\boldsymbol{H}}^T_k$ and $\tilde{\boldsymbol{R}}_k$ account for the uncertainties in measurement residual errors due to the state uncertainties and measurement noises, respectively.

Using the same derivation process in Eqs. (46)-(70), the new expression of the cross-correlation covariance matrix $\hat{\boldsymbol{P}}^{xz}_{k|k-1}$ can be obtained as

$$\hat{\boldsymbol{P}}^{xz}_{k|k-1} \approx \tilde{\boldsymbol{H}}^T_k\hat{\boldsymbol{P}}_{k|k-1} . \tag{71}$$

Recall that the expressions in Eqs. (70)-(71) correspond to the case of $n_{\mathrm{VBR}} = 1$. For the case where more than one VBR measurements is employed at epoch t_k, the matrixes $\tilde{\boldsymbol{H}}_k$ and $\tilde{\boldsymbol{R}}_k$ are rewritten as

$$\tilde{\boldsymbol{H}}_k = \begin{bmatrix} \boldsymbol{H}_{1,k} \\ \boldsymbol{H}_{2,k} - \frac{\boldsymbol{h}_2(\hat{\boldsymbol{x}}_k)}{\boldsymbol{h}_2(\hat{\boldsymbol{x}}_{k-\delta_1|k})}\boldsymbol{H}_{2,k-\delta_1}\left[\boldsymbol{\Phi}^{t_k}_{t_{k-\delta_1}}(\hat{\boldsymbol{x}}_{k|k-1})\right]^{-1} \\ \vdots \\ \boldsymbol{H}_{2,k} - \frac{\boldsymbol{h}_2(\hat{\boldsymbol{x}}_k)}{\boldsymbol{h}_2(\hat{\boldsymbol{x}}_{k-\delta_{n_{\mathrm{VBR}}}|k})}\boldsymbol{H}_{2,k-\delta_{n_{\mathrm{VBR}}}}\left[\boldsymbol{\Phi}^{t_k}_{t_{k-\delta_{n_{\mathrm{VBR}}}}}(\hat{\boldsymbol{x}}_{k|k-1})\right]^{-1} \end{bmatrix} \in \mathbb{R}^{(2+n_{\mathrm{VBR}})\times6} , \tag{72}$$

$$\tilde{\boldsymbol{R}}_k = \begin{bmatrix} \boldsymbol{R}_{1,k} & \mathbf{0}_{2\times1} & \cdots & \mathbf{0}_{2\times1} \\ \mathbf{0}_{1\times2} & (\hat{\rho}_{k-\delta_1|k})^2 P^{k-\delta_j}_k & \cdots & \mathbf{0}_{2\times1} \\ \vdots & \vdots & \ddots & \vdots \\ \mathbf{0}_{1\times2} & \mathbf{0}_{1\times2} & \cdots & (\hat{\rho}_{k-\delta_{n_{\mathrm{VBR}}}|k})^2 P^{k-\delta_j}_k \end{bmatrix} \in \mathbb{R}^{(2+n_{\mathrm{VBR}})\times(2+n_{\mathrm{VBR}})} . \tag{73}$$

Then, the predicted measurement covariance matrix $\hat{\boldsymbol{P}}^{zz}_{k|k-1}$ and cross-correlation covariance matrix $\hat{\boldsymbol{P}}^{xz}_{k|k-1}$ can be obtained by substituting Eqs. (72)-(73) into Eqs. (70)-(71). The the estimated state $\hat{\boldsymbol{x}}_k$ and the posterior covariance matrix $\hat{\boldsymbol{P}}_k$ can be obtained using Eqs. (13)-(15).

D. Overall procedure

An overview of the developed procedure for asteroid approach OD is shown in Fig. 3; the procedures of the EKF, the angle measurement generation, and VBR measurement generation are represented by yellow, purple, and green blocks, respectively. Note that the code to implement this is available in [41]. The user-defined parameters in the proposed method are the number of VBR measurements (as shown in Eq. (45)), n_{VBR}, and the number of the range ratio data selected for smoothing, M. It can be seen from Eqs. (22) and (45) that k-n_{VBR} should be no less than zero. Thus, $n_{\mathrm{VBR}} \leq k$ at epoch t_k. In addition, according to Eq. (23), the set $\mathcal{P}_k(\delta_j)$ contains k+1-δ_j elements. Therefore, given a value of δ_j ($j \in \mathbb{N}^+$ and $j \leq k$), the number selected data, M, should be no larger than k+1-δ_j. For example, at the epoch t_1, $j \leq 1$, $n_{\mathrm{VBR}} \leq 1$, and $M \leq 1$, which means that only one VBR measurement is available, and only one range ratio data can be employed for the LLP in Eqs. (38)-(41). At the epoch t_2, $j \leq 2$, $n_{\mathrm{VBR}} \leq 2$, and when $j = 1$ ($\delta_1 = 1$), $M \leq 2$, whereas when $j = 2$ ($\delta_2 = 2$), $M \leq 1$.

IV. Numerical Simulations

Several numerical simulations are presented to assess the performance of the proposed asteroid approach OD method. The simulations are performed on a laptop with a 2.5 GHz processor (12th Gen Intel(R) Core(TM) i5-12500H) and a 16 GB RAM. Note that the implementation is not optimized for efficiency.

A. Scenario

The approach phase of the asteroid Bennu is taken as an example to examine the performance of the proposed OD method. The initial epoch (t_0) is set as 26 September 2018, 19:15:30 UTC (2458388.30243056 Julian Date). The initial states of the spacecraft and the Bennu in the HEI frame are listed in Table 3 to four decimal places, and the approach OD simulation is carried over 14 days (336 hours) with a measurement interval of 1 hour. The dynamics in Eq. (2) are employed to describe the motion of both Bennu and spacecraft. Four perturbation bodies, the Earth, Earth's Moon, Mercury, and Mars, are considered for the dynamics in Eq. (2), as they have closer distance with the simulated objects than other bodies have. The area-to-mass ratios of the spacecraft and the asteroid are set as $4.038 \times 10^{-9}\,\mathrm{km}^2/\mathrm{kg}$ and $1.302 \times 10^{-11}\,\mathrm{km}^2/\mathrm{kg}$, respectively. The area-to-mass ratios are roughly obtained by dividing the area of the OSIRIS-Rex explorer (or asteroid Bennu) by its mass. The area and mass data of the OSIRIS-Rex explorer and asteroid Bennu come from [9]. In this work, the orbits (as well as the STM) are propagated using a Runge-Kutta (4,5) solver with a relative tolerance of 10^{-12} and an absolute tolerance of 10^{-12} [42].

The nominal trajectory and the time history of the relative distance between the spacecraft and the Bennu are presented in Fig. 4(a) and Fig. 4(b), respectively. In Fig. 4(a), Bennu is not shown to scale. The relative trajectory shown in Fig. 4(a) is near-linear, making the optical OD suffer from range ambiguity. It should be noted that the approach trajectory used in this paper is not the same trajectory in the true OSIRIS-REx mission, which contained four asteroid

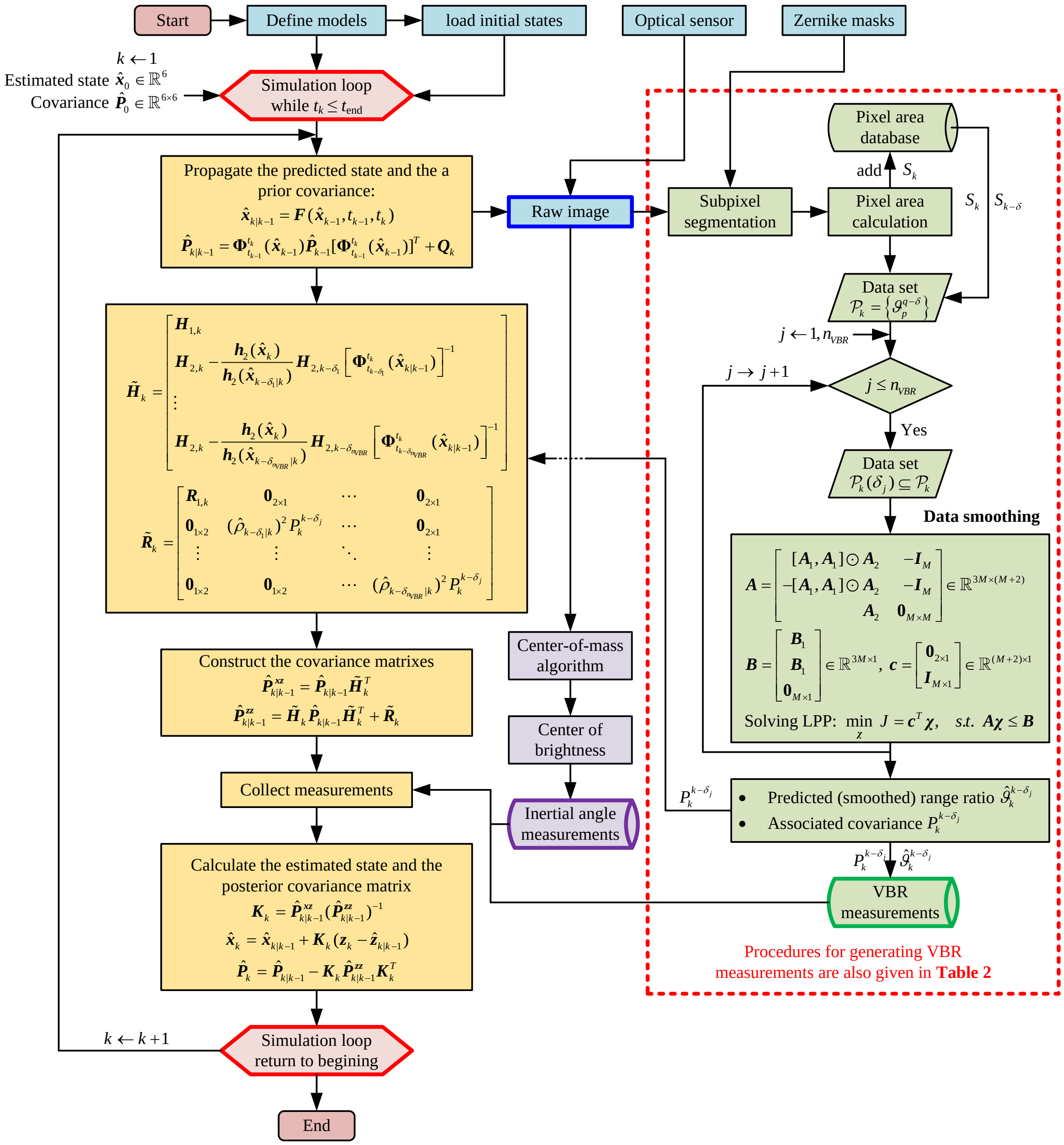

Fig. 3 Flowchart of the proposed method.

Table 3 The initial states of the spacecraft and the asteroid Bennu in the HEI frame

Object	Position (km)			Velocity (km/s)		
	x	y	z	$\dot{x}$	$\dot{y}$	$\dot{z}$
Bennu	128987502.9094	-101140857.3511	-57700694.7742	13.7847	20.4332	11.4878
Spacecraft	128986714.1768	-101134740.0474	-57698638.5856	13.7853	20.4282	11.4861

approach maneuvers (AAMs) to slow down the approach rate and correct the trajectory [10, 43]. As this numerical simulation aims to show the advantages of adding VBR measurements, a non-maneuver approach trajectory is desired to simplify the presentation of the method.

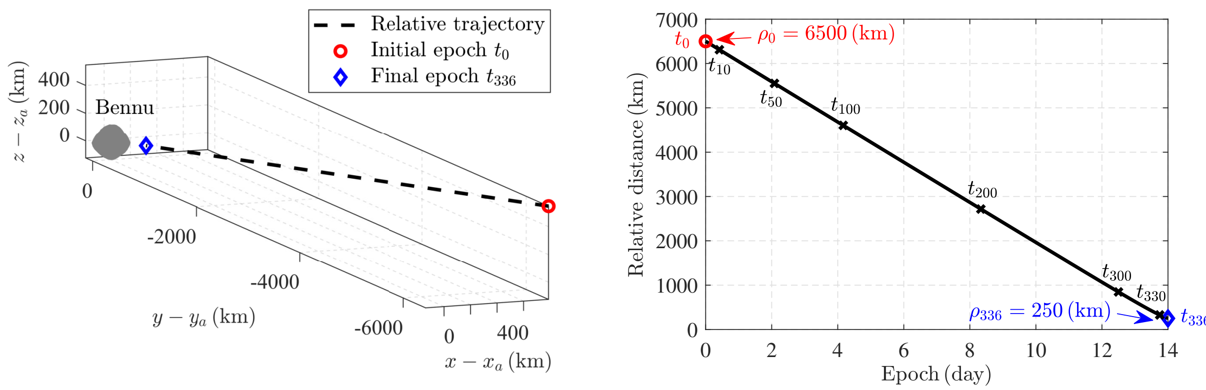

(a) Relative trajectory (b) Relative distance

Fig. 4 Nominal orbit of the approach phase.

The images of Bennu during the approach phase are rendered using a free software Blender†, with the 3D model of Bennu from NASA‡. The properties of the camera are set to match the properties of the PolyCam on-board OSIRIS-REx: Table 4. The spin of Bennu is considered, with the spin period set as 4.276 hours [9]. Bennu's equator is tilted by 176 deg [9]. A parallel ray light source is added to simulate sunlight, with the light strength, diffuse factor, specular factor, and volume factor set as 5, 1, 1, and 1 in Blender, respectively. When generating the images, the camera is pointed towards Bennu to make sure that the asteroid is always in the field of view.

Table 4 Properties of the camera simulated [10, 44]

Properties	PolyCam (at ∞)
IFOV (μrad/pixel)	13.5
Detector size (pixel)	1024×1024
Aperture (mm)	175
Focal length (mm)	630
Pixel size (microns)	8.5×8.5

Some of the rendered images are shown in Fig. 5. All the rendered images are available at [41]. In Fig. 5, the scale of each image is different, as such a pixel count scale for each image is shown. In addition, the ranges between the spacecraft and asteroid Bennu corresponding to the images in Fig. 5 are shown by black crosses in Fig. 4(b). It can be seen from Fig. 5 that Bennu occupies approximately 30 pixels in the image at a distance of 6500 km, whereas the number of pixels increases to more than 1000 at a distance of 250 km. Note that background noise, such as the star field,

†Available at `https://www.blender.org/` [retrieved on January 2025]
‡Available at `https://nasa3d.arc.nasa.gov/detail/bennu` [retrieved on January 2025]

is not considered when rendering the images, equivalent to the background noise having been eliminated with common image filtering algorithms such as the Gaussian filtering algorithm, median filtering algorithm, or bilateral filtering algorithm [45].

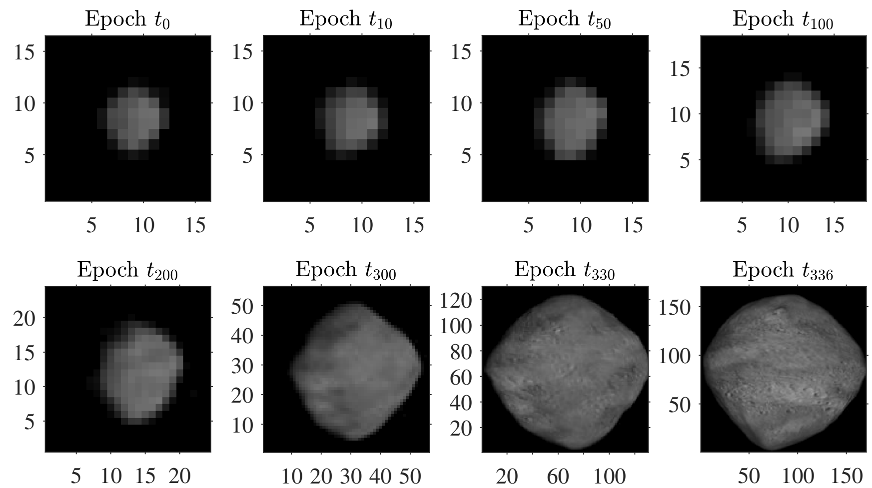

Fig. 5 Examples of the rendered images (axes are in pixels).

B. Measurement calculation results

The performance of the center-of-mass algorithm for asteroid centroid extraction, the subpixel edge detection algorithm, and the range ratio smoothing algorithm are analyzed in this section via numerical simulations. The outputs of the center-of-mass algorithm at different epochs are shown in Fig. 6, whose axes are in pixels. As expected, the true center does not coincide with the center of brightness due to irregular shape and illumination conditions. The STD of the angle measurement errors due to the residuals between the true center and the center of brightness is 2×10^{-5} rad for the right ascension and 3×10^{-6} rad for the declination. In addition, white noise, with STD of 10^{-4} rad, is added to the obtained right ascension and the declination to simulate attitude estimation errors. This leads to the choice of the angle measurement covariance $\boldsymbol{R}_{1,k}$ as

$$\boldsymbol{R}_{1,k} = \begin{bmatrix} 1.2^2 \times 10^{-8}\mathrm{rad}^2 & 0 \\ 0 & 1.03^2 \times 10^{-8}\mathrm{rad}^2 \end{bmatrix}. \tag{74}$$

The pixel area calculation results at the epochs t_0 and t_{50} are shown in Fig. 7. The raw images are displayed in Fig. 7(a) and Fig. 7(c), whereas the corresponding subpixel edges are shown in Fig. 7(b) and Fig. 7(d). In Fig. 7(b) and Fig. 7(d), the red crosses represent the subpixel edges detected by the Zernike moment algorithm (see step 2 in Fig. 1), and the pixel area of the asteroid on the image is obtained by computing the area of the polygon (the red areas). In this

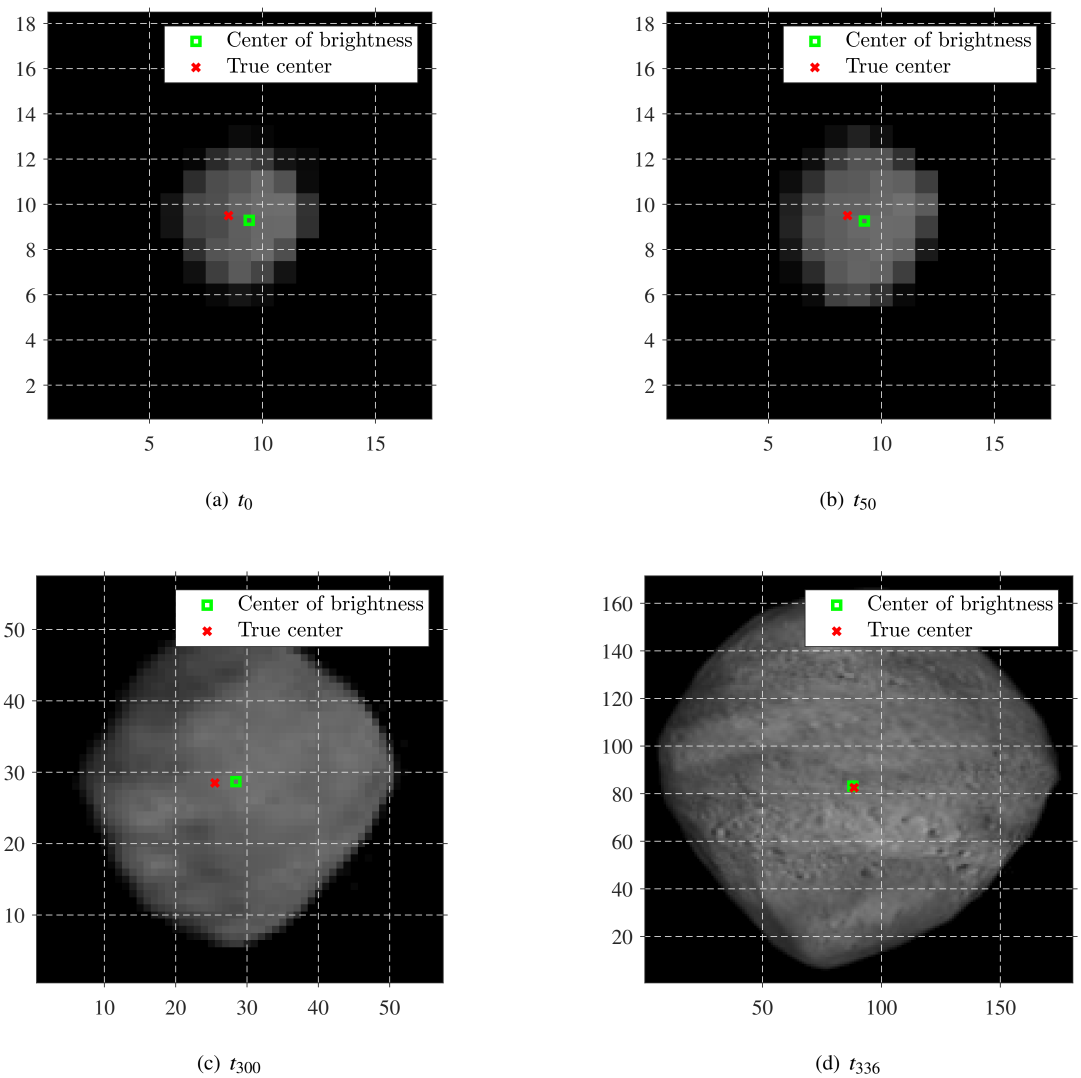

Fig. 6 Centroid extraction results using the center-of-mass algorithm.

work, $\eta = 0.1 \times 255$ (note that 255 is the maximal gray value of a pixel) is selected as the threshold to convert grayscale images to binary images (see step 1 in Fig. 1). Such a threshold value is selected after a trial-and-error procedure. Although background noises are not added to the image, noises also exist around the edges of the asteroid due to the limitation of the resolution ratio. These edge noises make the asteroid look blurry, and its size in the image is larger than it actually is. The thresholding process can help reduce the edge noises and improve the accuracy of pixel area calculation.

The range ratio data and covariance prediction results are shown in Fig. 8. The profiles of ϑ_k^{k-1} (the original range ratios predicted using Eq. (18)) and $\hat{\vartheta}_k^{k-1}$ (the smoothed range ratios obtained by solving the LLP in Eq. (41)) are shown in blue and green lines in Fig. 8(a). As a reference, the true range ratio, $\frac{\rho_k}{\rho_{k-1}}$, is represented by the black line in Fig. 8(a).

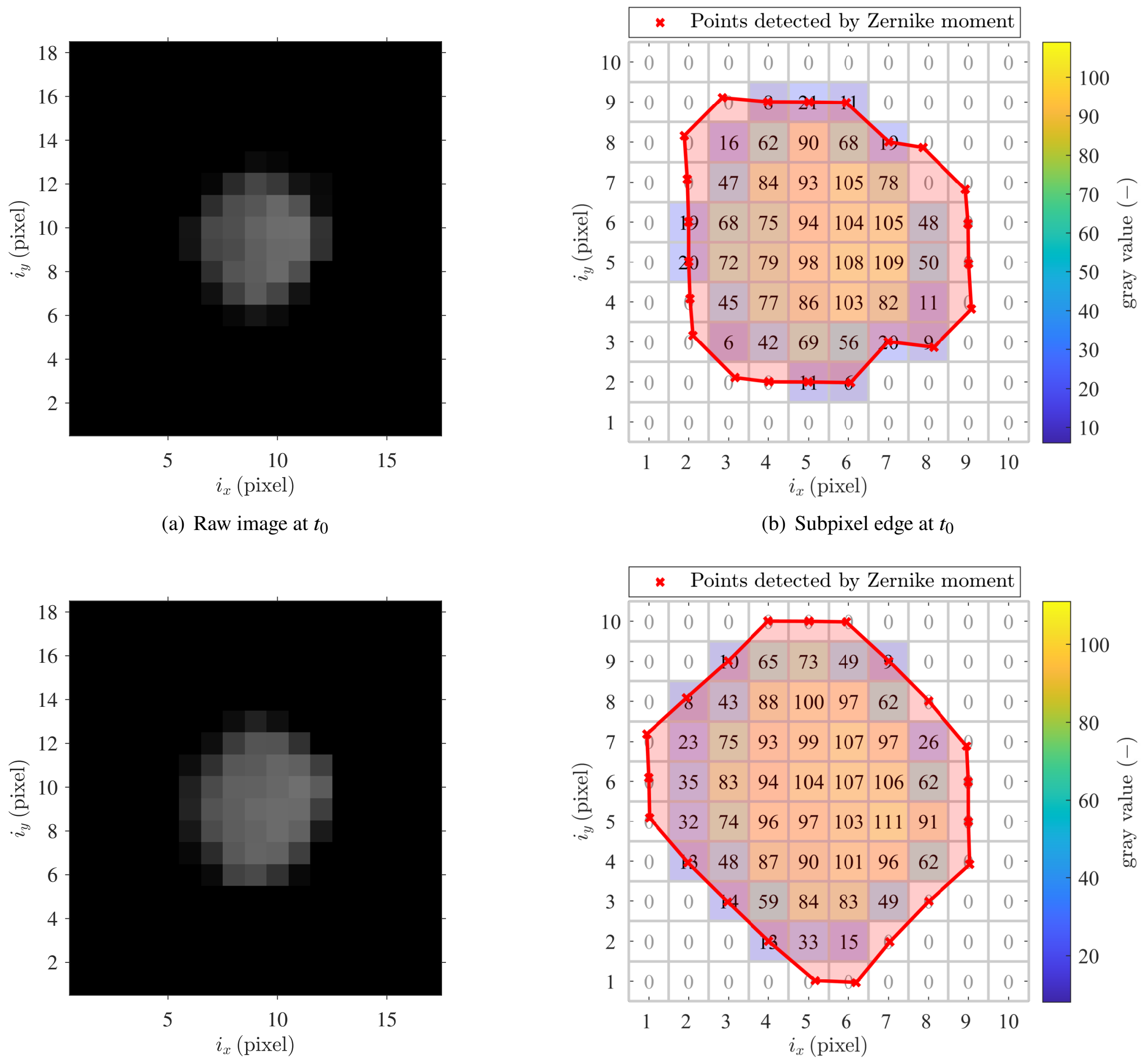

(a) Raw image at t_0 (b) Subpixel edge at t_0

(c) Raw image at t_{50} (d) Subpixel edge at t_{50}

Fig. 7 Pixel area calculation results.

The number of the range ratio data for smoothing, M, is set as

$$M = \begin{cases} k & k \leq 10 \\ 10 & \text{elsewise} \end{cases} . \tag{75}$$

In addition, Fig. 8(a) gives the smoothed range ratio data without the constraint in Eq. (33) (shown in red lines). The errors for the original and two smoothed range ratios with respect to the true data are plotted in Fig. 8(b). It can be seen from Fig. 8(b) that the maximal predicted error of the original range ratios is approximately 0.1, which, after smoothing with the constraint, decreases to no more than 0.05. The mean absolute errors of smoothing with and without the constraint are 0.0084 and 0.0116, respectively. Compared with smoothing without the constraint, adding a constraint

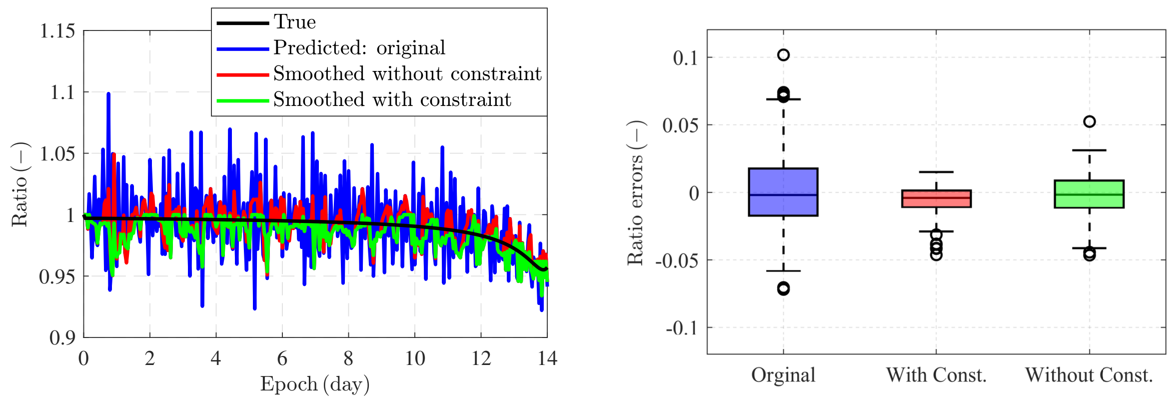

(a) Range ratio profiles (b) Errors

Fig. 8 Range ratio data preprocessing results.

like Eq. (33) improves the accuracy by approximately 27.59%. In addition, the green line (*i.e.*, after smoothing with the constraint) in Fig. 8(a) tends to underestimate the range ratio. This is because Eq. (33) always constrains the smoothed data to be smaller than 1.

The covariance predictions of the range ratio $\hat{\vartheta}_k^{k-1}$ (after smoothing with the constraint) are shown in Fig. 9, with the absolute errors and the predicted STD (Eq. (42)) represented by blue and red curves, respectively. The predicted STD profiles have similar tendencies and magnitudes, indicating that Eq. (42) can effectively predict the uncertainties of range ratios. Note that the range ratio errors are not evenly distributed. This is because the measurements are generated using rendered images, and non-Gaussian errors are inevitably carried over when calculating the pixel area and smoothing the data.

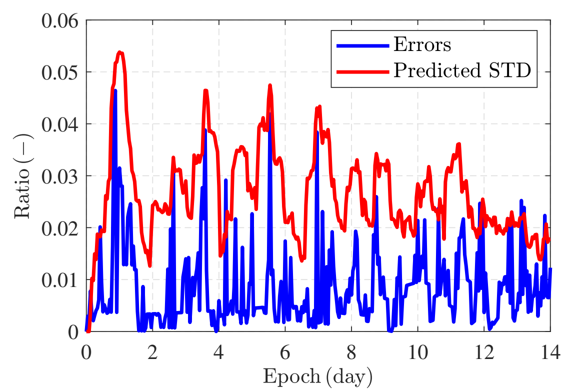

Fig. 9 Predicted standard deviation for the range ratio data.

C. Orbit determination performance analysis

The OD performance of the proposed method is validated on the example approach phase of the asteroid Bennu. Ephemeris errors are not added to Bennu's state ($\boldsymbol{r}_a$) in simulations here; however, a sensitivity analysis to such errors is presented in Sec. IV.D. In addition, during the implementation of orbit estimation, the EKF's dynamics model is set as exactly the same as that in Eq. (2). That is, no process noises are added as the physical properties (*e.g.*, the reflection coefficient) of the spacecraft can always be accurately measured in the designing process. however, in the numerical simulation, a process noise covariance matrix of $\boldsymbol{Q}_k = 10^{-14}\boldsymbol{I}_6$ is added to avoid potential numerical singularity, which is a normal step in implementing Kalman filters. Letting $\hat{\boldsymbol{P}}_0 = \text{diag}\left\{[\sigma_R^2, \sigma_R^2, \sigma_R^2, \sigma_V^2, \sigma_V^2, \sigma_V^2]\right\}$ be the covariance matrix of the initial estimation $\hat{\boldsymbol{x}}_0$, where σ_R and σ_V denote the position and velocity STD, respectively, two cases are simulated with their initial position and velocity STD listed in Table 5.

Table 5 Parameter settings of two cases simulated

Case	σ_R (km)	σ_V (km/s)
Case I	100	0.01
Case II	10	0.001

Before presenting the simulation results, a new frame, noted as the spacecraft-centered relative (SCR) frame, is defined. As shown in Fig. 10, the HEI and SCR frames are colored black and red, respectively. The origin of the SCR frame ($\tilde{O}$) is located in the (mass) center of the spacecraft (in this work, the spacecraft is considered as a point), with the $\tilde{x}$-axis pointing to the target asteroid (say, the line-of-sight [LOS] direction in Fig. 10), and the $\tilde{y}$- and $\tilde{z}$-axes vertical to the $\tilde{x}$-axis. In this paper, the $\tilde{y}$- and $\tilde{z}$-axes of the SCR frame are determined using Schmidt orthogonalization. The steps for generating such a SCR frame are detailed as follows. First, define a 3-dimensional unit matrix as $\boldsymbol{T} = \boldsymbol{I}_3 \in \mathbb{R}^{3\times3}$. Then, replace the first column of the unit matrix with the LOS direction and generate a new matrix $\boldsymbol{T}'$. Finally, perform Schmidt orthogonalization for the new matrix $\boldsymbol{T}'$ and generate matrix $\boldsymbol{T}''$. The directions along the $\tilde{x}$-, $\tilde{y}$- and $\tilde{z}$-axes (of the SCR frame) in the HEI frame are represented by the first, second, and third columns of the matrix $\boldsymbol{T}''$. In the defined SCR frame, the absolute value of the coordinate of the target asteroid along the $\tilde{x}$-axis is equivalent to the distance between the spacecraft and the asteroid.

1. Single case simulation results

A single OD simulation is performed based on case I in Table 5. As such, the initial guess ($\hat{\boldsymbol{x}}_0$) is off by 100 km for the position components and 0.01 km/s for the velocity components such that they lie on the boundary of the 1σ ellipsoid of the initial uncertainties. The time histories of the estimated errors of case I using angle-only measurements are depicted in Fig. 11. The estimated errors in the inertial frame are shown in Fig. 11(a), whereas Fig. 11(b) gives the estimated errors in the relative frame. It is seen from Fig. 11 that the estimated errors converge after approximately 6

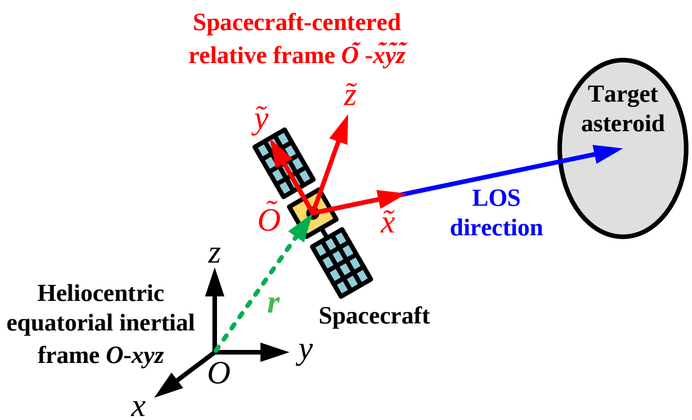

Fig. 10 An illustration of the spacecraft-centered relative frame.

days. The position errors increase up to t = 2 days before stabilizing. This is because the position errors are affected by the propagation of velocity components. As shown in Fig. 11, the velocity errors converge at around t = 2 days, before which the position errors continuously grow. Note that measurements at the initial epoch are employed, which means that at the initial epoch, only the measurement update procedure (of EKF) is performed (in other epochs, both time and measurement update procedures are performed). This also explains why the position errors at the initial epoch are not 100 km. The maximal position and velocity errors are on the orders of 1000 km and 10 m/s, respectively. It is also interesting to see from Fig. 11(b) that the estimated errors along the $\tilde{x}$-axis (represented by blue lines) converge much slower than the errors along the other two axes. Recall that the coordinate along the $\tilde{x}$-axis is equivalent to the range between the spacecraft and the asteroid. Such a result is expected due to the range ambiguity of angle-only measurement.

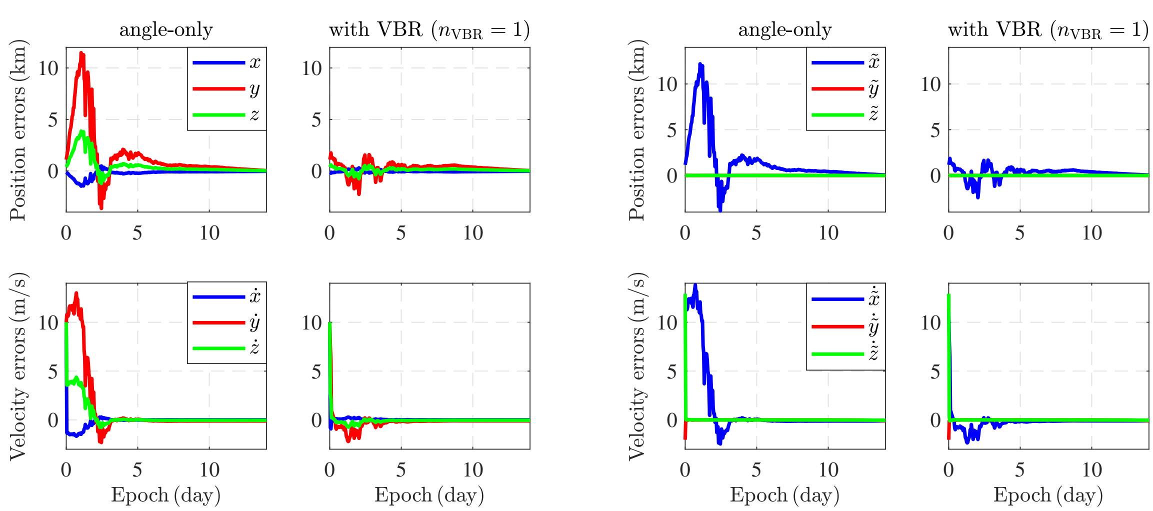

(a) HEI frame

(b) SCR frame

Fig. 11 Single-run estimated errors.

Consider now the same initial guess and covariance but with a VBR measurement per epoch ($n_{\text{VBR}} = 1$) to improve the approach OD performance. At each epoch t_k, a VBR measurement is constructed by determining the range ratio for the current epoch (*i.e.*, t_k) with respect to the one right before (*i.e.*, t_{k-1}). Thus, the VBR measurement at the epoch t_k is given as $z_2(\boldsymbol{x}_k; \hat{\boldsymbol{x}}_k, \delta_1 = 1)$. The time histories of estimated errors using the angle and one VBR measurement per epoch are also presented in Fig. 11. As expected, the estimated errors with one VBR measurement per epoch converge much faster than the estimated errors with the angle-only measurement. By adding one VBR measurement per epoch, the maximal position estimated error decreases to no more than 250 km, which is approximately one-fifth of that using angle-only measurements. Re-note that n_{VBR} is the number of VBR measurements employed per simulated epoch; that is, $n_{\text{VBR}} = 1$ doesn't mean that one single VBR measurement is repeatedly employed at all time steps. We will not emphasize this in the following of this paper for simplicity.

2. Monte Carlo simulation results

Monte Carlo (MC) studies are performed to further assess the performance of the proposed method. One hundred MC runs are performed for each case given in Table 3. In each MC run, the initial guess $\hat{\boldsymbol{x}}_0$ is randomly generated from the distribution $\mathcal{N}(\hat{\boldsymbol{x}}_0; \boldsymbol{x}_0, \hat{\boldsymbol{P}}_0)$ with $\boldsymbol{x}_0$ being the true initial state (the true initial state is listed in Table 3) and $\hat{\boldsymbol{P}}_0 = \text{diag}\left\{[\sigma_R^2, \sigma_R^2, \sigma_R^2, \sigma_V^2, \sigma_V^2, \sigma_V^2]\right\}$ being the initial covariance (the values of σ_R and σ_V are listed in Table 5). In addition, the attitude estimation errors are randomly generated in the angle measurements in each run (with the STD of the attitude errors being 10^{-4} rad). Note that the same images (as shown in Fig. 5) are employed for different runs, as no noises are considered when rendering these images, ensuring only uncertainties in the initial orbit estimation and attitude estimation, rather than those from image processing, are considered herein. For case I, the position and velocity estimated errors (in the HEI frame) of 100 MC runs using angle-only measurements are represented by grey lines in the left subplots in Fig. 12(a) and Fig. 12(b), respectively. Moreover, Fig. 13 gives the MC results of the case II. In Fig. 12 and Fig. 13, $\boldsymbol{e} = [e_x, e_y, e_z]^T$ (see Fig. 12(a) and Fig. 13(a)) and $\dot{\boldsymbol{e}} = [\dot{e}_x, \dot{e}_y, \dot{e}_z]^T$ (see Fig. 12(b) and Fig. 13(b)) denote the position and velocity estimated errors, respectively. Additionally, at each epoch, two STDs are analyzed: one is the statistical STD, and the other is the predicted STD. The predicted STDs over time are obtained from the EKF's measurement update step, say, the square root of the diagonal elements of the posterior covariance matrix in Eq. (15). The statistical STDs are obtained based on the 100 MC runs, defined as

$$\text{STD}_\Delta(t_k) = \sqrt{\frac{\sum_{i=1}^{n_{\text{MC}}} \left(\Delta_{k,i} - \bar{\Delta}_k\right)^2}{n_{\text{MC}} - 1}}, \Delta \in \{e_x, e_y, e_z, \dot{e}_x, \dot{e}_y, \dot{e}_z\}, \tag{76}$$

where $\Delta_{k,i}$ denote the estimated errors (in HEI frame) at the epoch t_k in the i-th MC run, respectively, $n_{\text{MC}} = 100$ is the total number of MC runs, and $\bar{\Delta}_k = \frac{\sum_{i=1}^{n_{\text{MC}}} \Delta_{k,i}}{n_{\text{MC}}}$ represents the mean estimated errors. In Fig. 12 and Fig. 13, the statistical and predicted 3σ (three times the STDs) bounds are shown by blue and red lines, respectively. One can see from Fig. 12 and Fig. 13 that at the beginning, the statistical and predicted STDs are in good agreement. However, when the errors converge (*e.g.*, 10 days $\leq t \leq$ 14 days), these two STDs don't match well. Our explanation is given as follows. As shown in Eqs. (12)-(15), the posterior covariance matrix $\hat{\boldsymbol{P}}_k$ is mainly affected by the measurement noise covariance $\boldsymbol{R}_k$ when the estimated errors are very small. In this work, the angle measurements come from implementing the center-of-mass algorithm on the rendered pictures; thus, the angle measurement noises are not Gaussian distributed, and a covariance $\boldsymbol{R}_k$ cannot accurately capture the distribution.

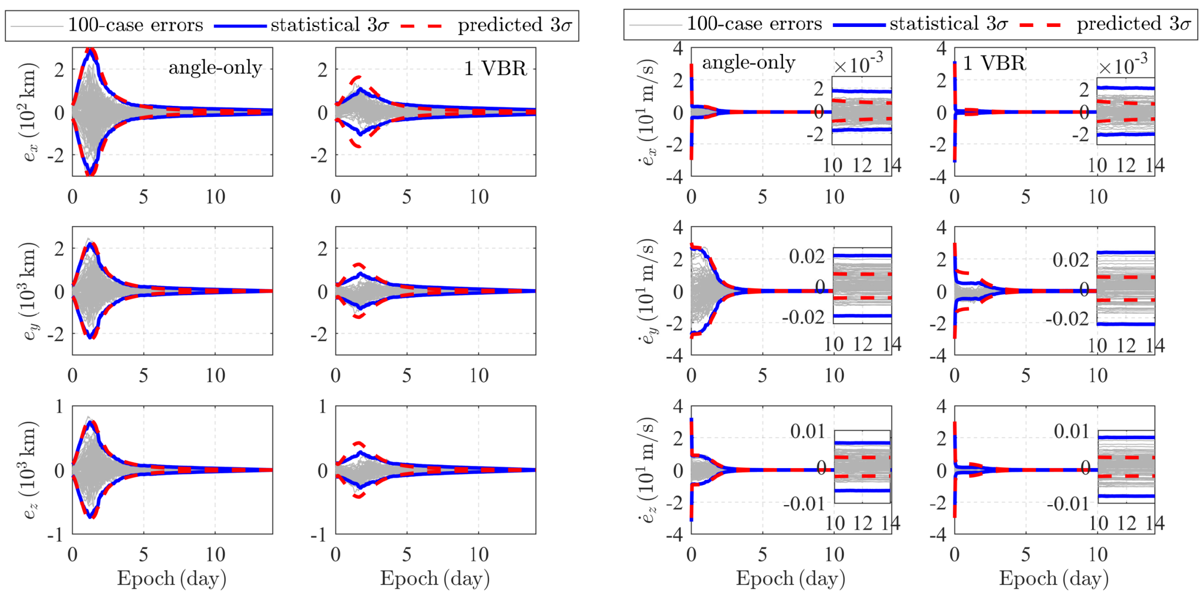

(a) Position (b) Velocity

Fig. 12 Monte Carlo simulation results of Case I.

The right subplots of Fig. 12(a), Fig. 12(b), Fig. 13(a), and Fig. 13(b) present the MC results with one additional VBR measurement per epoch. As shown in Fig. 12(a) and Fig. 12(b), in case I, by adding one VBR measurement per epoch, the estimated errors are significantly reduced, especially for the first 5 days (*i.e.*, $t < 5$ days). However, slight improvements benefiting from the VBR measurements are shown for case II (see Fig. 13(a), and Fig. 13(b)). The reasons for different levels of improvement in the two cases will be discussed in the second half of this subsection. In addition, using the proposed method (*i.e.*, with one VBR measurement per epoch), the statistical and predicted $s\sigma$ curves match well in case II, while they are in bad agreement in case II. This is related to the uncertainty quantification capacity of the proposed method, which will be further analyzed and discussed in Sec. IV.C.4, and this subsection mainly focuses on investigating the accuracy and convergence performances.

Three metrics are employed to compare the OD performance with and without VBR measurements: the STD of the estimated errors, the averaged STD (ASTD), and the time-weighted STD (TWSDT). Here, the STDs refer to the

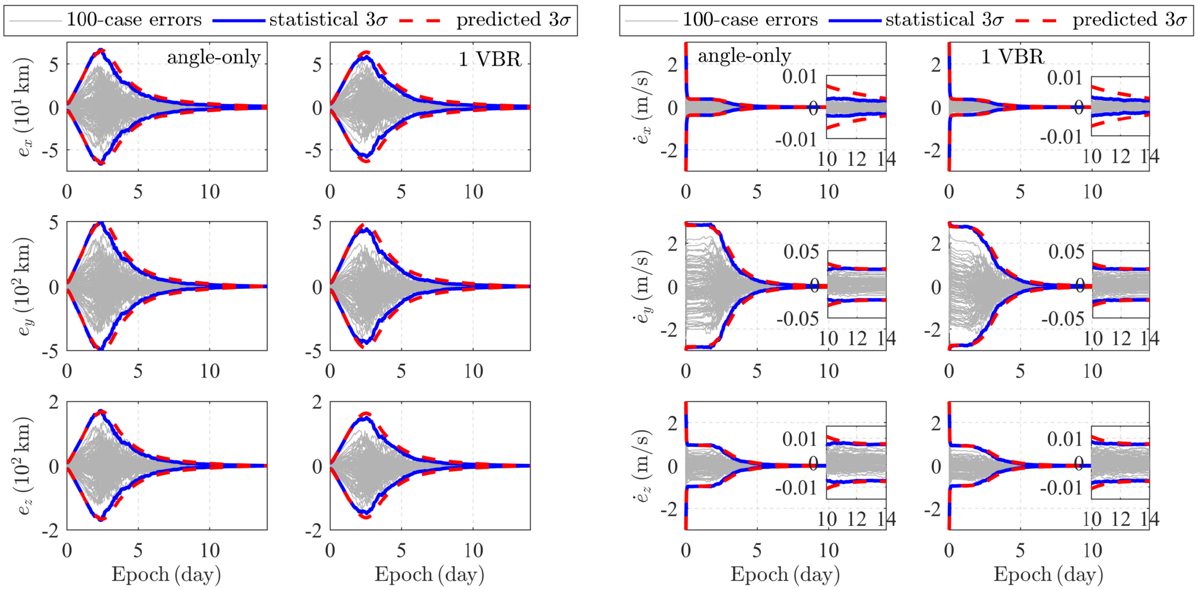

(a) Position (b) Velocity

Fig. 13 Monte Carlo simulation results of Case II.

statistical ones. The definition of the statistical STD is shown in Eq. (76), whereas the mathematical models of the remaining two metrics are given as

$$\mathrm{ASTD}(\Delta) = \frac{\sum_{k=1}^{N} \mathrm{STD}_{\Delta}(t_k)}{N}, \Delta \in \{e_x, e_y, e_z, \dot{e}_x, \dot{e}_y, \dot{e}_z\}, \tag{77}$$

$$\mathrm{TWSTD}(\Delta) = \sum_{k=1}^{N} t_k \times \mathrm{STD}_{\Delta}(t_k), \Delta \in \{e_x, e_y, e_z, \dot{e}_x, \dot{e}_y, \dot{e}_z\}, \tag{78}$$

where $N = 336$ is the total number of epochs. The STD and ASTD are employed to evaluate the accuracy of different methods. Smaller STD and ASTD indicate smaller estimated errors and better accuracy. The TWSTD is used to assess the convergence performance. A method with smaller TWSTD converges faster, as it has smaller estimated errors in earlier epochs.

The STD profiles using angle-only measurements, angle and one VBR (*i.e.*, $n_{\mathrm{VBR}} = 1$) measurements, and angle and five VBR (*i.e.*, $n_{\mathrm{VBR}} = 5$) measurements are shown in Fig. 14. The ASTD and TWSTD results are detailed in Table 6, Table 7, Table 8, and Table 9. It can be seen from Fig. 14 that using VBR measurements can improve both estimated accuracy and convergence (see the results of method "Angle and VBR (with Eq. (72))"). The improvement becomes more remarkable when more VBR measurements are employed (n_{VBR} becomes larger). Similar results can be found in Table 6, Table 7, Table 8, and Table 9. As shown in Table 6 and Table 7, for case I, the averaged STDs along the y-axis using angle-only measurements, angle and one VBR measurements, and angle and five VBR measurements are 124.7648 km, 77.8539 km, and 51.5626 km, respectively, and the time-weighted STDs along y-axis using these three types of measurements is 1410.3536 km·day, 783.4698 km·day, and 478.7245 km·day, respectively. When one VBR measurement is added, the values of the ASTDs and TWSTDs (along the y-axis) are reduced by 37.5995% and 44.4487%, respectively, whereas when five VBR measurements are employed, the values of these two metrics (along the y-axis) is decreased by 58.6722% and 66.0564%, respectively.

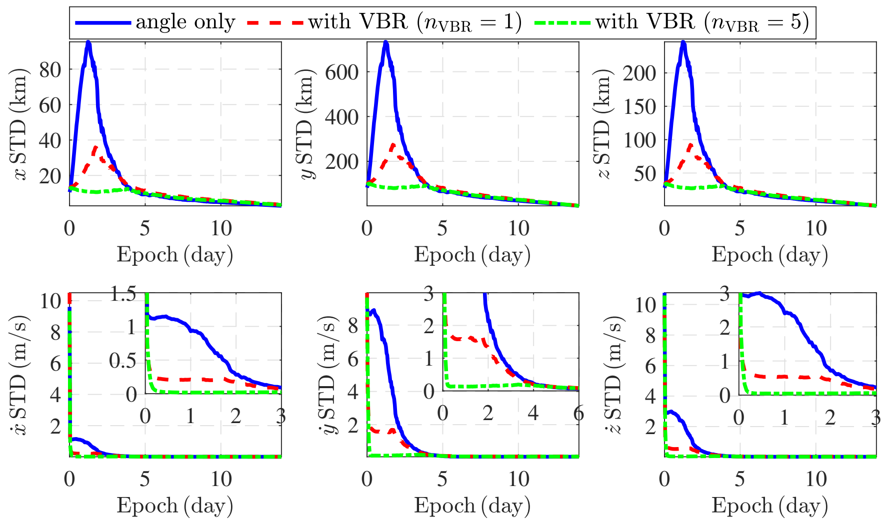

(a) Case I

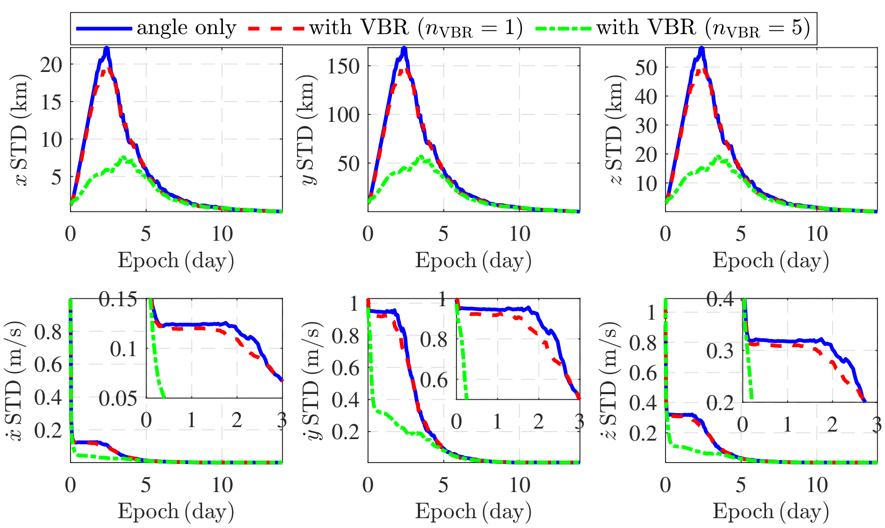

(b) Case II

Fig. 14 Time histories of the STDs using different types of measurements (HEI frame).

To show the performance of the derived expressions for the cross-correlation covariance matrix and the predicted measurement covariance matrix (Eq. (72)), Table 6, Table 7, Table 8, and Table 9 compare the MC simulation results of methods with and without (*i.e.*, $\tilde{\boldsymbol{H}}_k = [\boldsymbol{H}_{1,k}, \boldsymbol{H}_{2,k}, \cdots, \boldsymbol{H}_{2,k}] \in \mathbb{R}^{(2+n_{\mathrm{VBR}})\times 6}$) these newly derived covariance expressions. It is seen from these four tables that both the accuracy and the convergence performances degrade

Table 6 ASTD results of case I using different methods (HEI frame)

Methods	n_{VBR}	Position (km)			Velocity (km/s)		
		x	y	z	$\dot{x}$	$\dot{y}$	$\dot{z}$
Angle only	0	17.3633	124.7648	42.0902	0.1732	1.1476	0.4083
Angle and VBR (with Eq. (72))	1	11.4972	77.8539	26.3503	0.0803	0.4164	0.1578
	5	7.9781	51.5626	17.4993	0.0436	0.1605	0.0757
Angle and VBR (without Eq. (72))	1	78.7585	448.1978	153.8172	0.3381	1.8256	0.6522
	5	13.4138	76.8231	26.2692	0.0591	0.2694	0.1130
Takahashi's method	0	15.3646	106.5900	36.0265	0.1534	1.0139	0.3650

Table 7 TWSTD results of case I using different methods (HEI frame)

Methods	n_{VBR}	Position (km·day)			Velocity (km·day/s)		
		x	y	z	$\dot{x}$	$\dot{y}$	$\dot{z}$
Angle only	0	188.2264	1410.3536	474.7454	2.2348	14.4962	5.1914
Angle and VBR (with Eq. (72))	1	107.5533	783.4698	264.1119	1.0122	4.8228	1.8730
	5	67.2858	478.7245	161.5832	0.5487	1.6201	0.8526
Angle and VBR (without Eq. (72))	1	452.7732	3037.3828	1029.4527	2.1384	12.5649	4.5775
	5	89.1455	603.3649	204.1794	0.7083	2.6544	1.2151
Takahashi's method	0	154.7152	1143.6715	385.2397	1.9841	12.7637	4.6323

Table 8 ASTD results of case II using different methods (HEI frame)

Methods	n_{VBR}	Position (km)			Velocity (km/s)		
		x	y	z	$\dot{x}$	$\dot{y}$	$\dot{z}$
Angle only	0	5.3671	39.3311	13.2549	0.0341	0.2323	0.0802
Angle and VBR (with Eq. (72))	1	5.0720	37.1670	12.5223	0.0327	0.2234	0.0774
	5	2.6696	18.9527	6.3998	0.0165	0.0996	0.0362
Angle and VBR (without Eq. (72))	1	18.1024	114.2608	38.8305	0.0492	0.3211	0.1105
	5	10.3473	58.3468	19.9781	0.0258	0.1525	0.0535
Takahashi's method	0	4.9227	35.9641	12.1201	0.0319	0.2174	0.0756

Table 9 TWSTD results of case II using different methods (HEI frame)

Methods	n_{VBR}	Position (km·day)			Velocity (km·day/s)		
		x	y	z	$\dot{x}$	$\dot{y}$	$\dot{z}$
Angle only	0	56.9139	425.2984	143.1805	0.4147	2.7793	0.9639
Angle and VBR (with Eq. (72))	1	53.7083	401.4775	135.1217	0.3976	2.6723	0.9304
	5	25.8273	189.6818	63.9353	0.1994	1.1529	0.4258
Angle and VBR (without Eq. (72))	1	132.4433	911.2068	308.0972	0.4981	3.1587	1.0988
	5	61.9448	405.7041	137.6266	0.2457	1.3807	0.4989
Takahashi's method	0	51.8668	387.2340	130.3564	0.3880	2.6019	0.9101

considerably when the derived covariance expressions are not used. The averaged STDs of the proposed method are approximately one order of magnitude smaller than those of the method without using the derived covariance expressions (see Averaged STD results in Table 8). This degradation is caused by the uncertainties related to the VBR measurements not being accurately predicted if the time-series dependency is not considered.

It is interesting to find from Fig. 14(a) that for case II, the gain obtained from the VBR measurements seems to be weaker than that in case I. For case II, the ASTDs along the y-axis are reduced by 5.5% and 51.8% using one and five VBR measurements, respectively (as a comparison, the reduction ratios of case I are 37.6% and 58.7%). This can be understood as, the VBR measurement proposed in this work is not an 'accurate' measurement, rather it relies on the range ratios obtained from the pixel area of the asteroid in the images. Its accuracy is much poorer than the range measurement obtained using traditional sensors such as a laser range finder. As shown in Fig. 8(b), the range ratio errors at the first several epochs are on the order of 0.01. Therefore, at the first several epochs, with a distance of 6500 km, the VBR measurement error is approximately 65 km. The magnitude of the VBR measurement is larger than that of the initial position uncertainties in case II (10 km). Thus, the improvements of the VBR measurements on the approach OD performance are limited. However, case I has larger initial uncertainties (100 km), where remarkable improvements can be gained using VBR measurements. That's also the reason why the accuracy with VBR measurements is more similar to the angle-only case for $t > 5$ days in Fig. 14. The VBR measurements still provide extra information at those points; however, such information is almost useless for the OD due to its large errors.

3. *Comparison with an existing improvement method*

The proposed method can be compared with Takahashi's method [13]. Takahashi *et al.* handled the range ambiguity of angle-only measurements using angle size measurements. The mathematical model of the angle size of the asteroid is expressed as

$$h_3(\boldsymbol{x}_k) = \frac{R}{\rho_k}\,, \tag{79}$$

where $h_3(\boldsymbol{x}_k)$ stands for the angle size measurement model, ρ_k represents the range between the spacecraft and asteroid at epoch t_k, and R is the asteroid's mean radius. In Takahashi's method, the asteroid's mean radius is added to the state vector to be estimated, considering that the size of the asteroid is unknown. The state vector is then augmented as

$$\boldsymbol{X} = [x, y, z, \dot{x}, \dot{y}, \dot{z}, R] \in \mathbb{R}^7\,. \tag{80}$$

The angle size measurement contains the range information, which can alleviate the range ambiguity to a certain extent. In this simulation, the angle size measurement is obtained by fitting the asteroid's area projected on the image as a circle and calculating the mean radius, given by

$$z_3(\boldsymbol{x}_k) = h_3(\boldsymbol{x}_k) + \varepsilon_{3,k} = \sqrt{\frac{S_k}{\pi}}\,, \tag{81}$$

where $z_3(\boldsymbol{x}_k)$ is the angle size measurement obtained using the rendered images, $\varepsilon_{3,k}$ denotes the angle size measurement noise, and S_k (unit: rad^2) represents the asteroid's area projected on the image. The true asteroid's mean radius is given as $R = 246\,\mathrm{m}$. The initial estimated asteroid's mean radius is set as $\hat{R} = 0.9R$, and the initial covariance of R is given as $P(R) = (0.1R)^2$. The covariance of the angle size measurement is set as $\boldsymbol{R}_3 = 13.5^2\ \mu\mathrm{rad}^2$.

The corresponding results from Takahashi's method are listed in Table 6, Table 7, Table 8, and Table 9 as a comparison. Takahashi's method outperforms the conventional angle-only approach in terms of accuracy and convergence, and its performance is poorer than that of the proposed method. Three reasons related to the poor performance of Takahashi's method are identified. First, Takahashi's method models the asteroid as a sphere, which is too simple for the irregular shape model used in the simulation (as shown in Fig. 5). Second, simply assuming the angle size measurement errors as Gaussian-distributes ($\boldsymbol{R}_3 = 13.5^2\ \mu\mathrm{rad}^2$) may be too optimistic, and a more sophisticated error model is desired due to the irregular shape of the asteroid. Third, Takahashi's method introduces a new parameter (the asteroid's mean radius) to construct the angle measurement. Although a new measurement is brought in, it increases the state dimension of the OD system, and thus, the algorithm needs more time to converge.

4. Analysis of uncertainty quantification capacity

The Mahalanobis distance (MD) is taken as a metric to evaluate the uncertainty quantification capacity of the proposed method. The MD at the epoch t_k is defined as

$$\mathrm{MD}(t_k) = \sqrt{(\hat{\boldsymbol{x}}_k - \boldsymbol{x}_k)^T \boldsymbol{P}_k^{-1} (\hat{\boldsymbol{x}}_k - \boldsymbol{x}_k)}\,, \tag{82}$$

where $\hat{\boldsymbol{x}}_k$ and $\boldsymbol{x}_k$ represent the estimated and true states at the epoch t_k, and $\hat{\boldsymbol{P}}_k$ is the state covariance predicted by the EKF (using Eq. (15)). An MD closer to the square root of the problem dimension (*i.e.*, $\sqrt{6}$ for the OD problem investigated in the work) indicates a better uncertainty quantification capacity [46].

Based on the 100 MC runs, the mean MDs are obtained for the proposed method and competitive methods (say, angle-only). Figure 15 gives the mean MD results with time. As references, the desired MD (*i.e.*, MD = $\sqrt{6}$) is shown by grey dashed lines in Fig. 15. As shown in Fig. 15(a), in case II (with larger initial uncertainties), adding additional VBR measurements leads to larger MDs than the angle-only results, indicating that the EKF's uncertainty quantification capacity is poorer. However, in case II, adding one VBR per epoch doesn't significantly impact the MD results (see Fig. 15(b)), which also matches the results in Fig. 13. Our explanation is given as follows. When deriving new expressions for the covariances $\hat{\boldsymbol{P}}^{zz}_{k|k-1}$ and $\hat{\boldsymbol{P}}^{xz}_{k|k-1}$, a linear approximation is employed, as shown in Eq. (63). The linear solution's predicted errors grow as the magnitude of the state deviation $\delta \boldsymbol{x}_k$ increases, leading to a poorer accuracy of the covariances $\hat{\boldsymbol{P}}^{zz}_{k|k-1}$ and $\hat{\boldsymbol{P}}^{xz}_{k|k-1}$. A simple simulation is implemented to validate the explanation. Let $k = 1$ and take the epoch t_1 as an example. Random errors are added to the true state $\boldsymbol{x}_1$, with the position and velocity STDs being $10\lambda_{P_1}$ km and $1\lambda_{P_1}$ m/s, respectively. One hundred MC runs are carried out, and the mean relative errors (MREs) are computed after determining the relative errors of the linear solution (say, Eq. (64)) in each MC run. As shown in Fig. 16, the MREs increase as the magnitude of estimation uncertainties (*i.e.*, $\delta \boldsymbol{x}_1$) become larger. When, $\lambda_{P_1} = 100$, the MREs are approximately 50%. As shown in Fig. 12, it's possible that the position errors reach 1000 km in the first case. The accuracy of the linear approximation can be further improved by considering high-order terms, such as implementing the VBR measurements in a high-order EKF framework [47, 48].

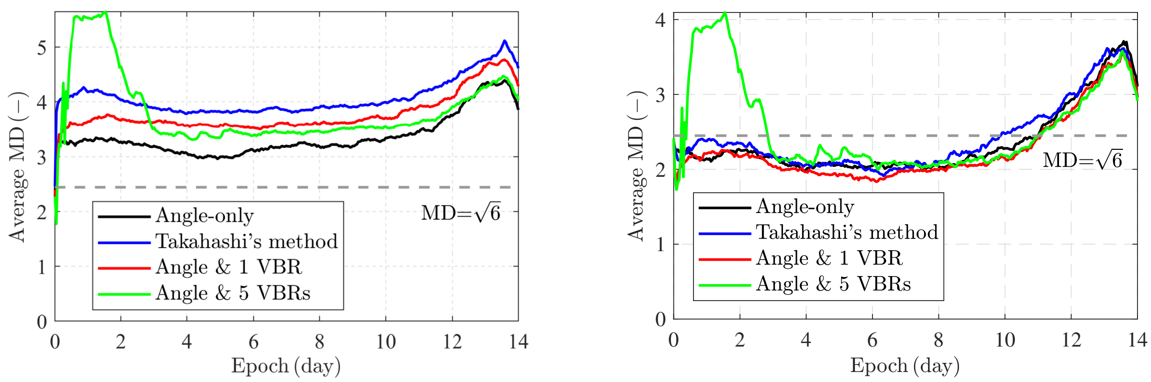

(a) Case I

(b) Case II

Fig. 15 Mahalanobis distance results of the MC simulation.

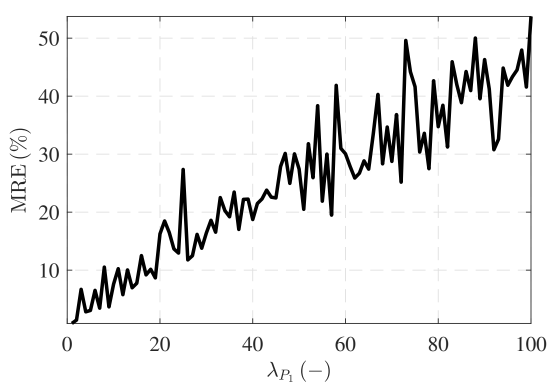

Fig. 16 Predicted errors of the VBR derivative under different levels of estimation uncertainty.

Another thing that should be mentioned is that when the number of VBR measurements increases, the EKF's uncertainty quantification performance degrades. As shown by green lines in Fig. 15, using five VBR measurements per epoch leads to a much larger MD, indicating that the predicted covariance is smaller than it should be. This is because when $n_{\mathrm{VBR}} > 1$, the pixel area information, in fact, is repeatedly employed during the filter process. However, the Kalman filter assumes that observations are independent. Reusing a measurement treats it as multiple independent inputs, which will reinforce its effect on the orbital state estimation, artificially amplify its influence, and ultimately underestimate uncertainty.

5. Computational cost analysis

Recalling that the implementation is not optimized for efficiency, the one-step computational costs of different methods are provided in Table 10 as a means of comparison. The time costs of centroid extraction and pixel area calculation are approximately 0.32 milliseconds and 2.41 milliseconds, respectively. The one-step computational time of the angle-only method is 8.04 milliseconds. The computational time increases by approximately 33.96% and 144.29% when adding one VBR measurement and five VBR measurements, respectively. The increased computational cost comes from the pixel area calculation and the integrations of the STM $\boldsymbol{\Phi}_{t_{k-\delta_j}}^{t_k}(\hat{\boldsymbol{x}}_{k|k-1})$ (as shown in Eq. (60)). In addition, the proposed method's benefits over that of Takahashi's method incur an increased computational cost.

Table 10 Computational costs of different methods

Methods	n_{VBR}	One-step computational cost (millisecond)			
		Centroid extraction	Pixel area calculation	One-step estimation	Total
Angle only	0	0.3089	-	8.0465	8.3555
Angle and VBR	1	0.3260	2.4107	8.4565	11.1933
	5	0.3117	2.2913	17.8089	20.4120
Takahashi's method	0	0.2508	2.0920	6.7991	9.1420

D. Sensitivity analysis

The simulation results are obtained by assuming that the true state of the asteroid is known. A sensitivity analysis is performed to analyze the influences of the ephemeris errors on the performance of the proposed method. Gaussian-distributed ephemeris errors are added at the initial epoch. The initial estimated state of the asteroid ($\hat{\boldsymbol{x}}_a(t_0)$) is randomly selected from the Gaussian distribution $\mathcal{N}(\hat{\boldsymbol{x}}_a(t_0); \boldsymbol{x}_a(t_0), \boldsymbol{P}_a(t_0))$, where $\boldsymbol{x}_a(t_0)$ represents the true initial state of the asteroid (listed in Table 3), and $\boldsymbol{P}_a(t_0)$ is the covariance, given by

$$\boldsymbol{P}_a(t_0) = \lambda^2 \mathrm{diag}\{[\boldsymbol{x}_a(t_0)]^2\}, \tag{83}$$

in which λ is a user-defined factor. The estimated state of the asteroid at any given epoch t, $\hat{\boldsymbol{x}}_a(t)$, can be obtained by propagating the initial estimated state $\hat{\boldsymbol{x}}_a(t_0)$ using the dynamics in Eq. (2).

Given the state estimation $\hat{\boldsymbol{x}}_k$ at the epoch t_k, the estimated state relative to the asteroid can be expressed as

$$\hat{\boldsymbol{x}}_k^{s/a} = \hat{\boldsymbol{x}}_k - \hat{\boldsymbol{x}}_a(t_k)\,, \tag{84}$$

where the superscript s/a represents the state of the spacecraft relative to the asteroid. The true spacecraft state relative to the asteroid is given as

$$\boldsymbol{x}_k^{s/a} = \boldsymbol{x}_k - \boldsymbol{x}_a(t_k)\,. \tag{85}$$

The residual error between Eq. (84) and Eq. (85) can be defined as

$$\boldsymbol{e}_k^{s/a} = \hat{\boldsymbol{x}}_k^{s/a} - \boldsymbol{x}_k^{s/a} = \underbrace{\hat{\boldsymbol{x}}_k - \boldsymbol{x}_k}_{\boldsymbol{e}_k} - \underbrace{\hat{\boldsymbol{x}}_a(t_k) - \boldsymbol{x}_a(t_k)}_{\boldsymbol{e}_a(t_k)}\,. \tag{86}$$

where $\boldsymbol{e}_k^{s/a}$ denotes the relative estimated error, $\boldsymbol{e}_k = \hat{\boldsymbol{x}}_k - \boldsymbol{x}_k$ and $\boldsymbol{e}_a(t_k) = \hat{\boldsymbol{x}}_a(t_k) - \boldsymbol{x}_a(t_k)$ represents the state estimated error of the spacecraft and the ephemeris error of the asteroid at the epoch t_k, respectively.

The relative estimated error $\boldsymbol{e}_k^{s/a}$, rather than the estimated error $\boldsymbol{e}_k$, is employed to evaluate the performance of the proposed method in the presence of ephemeris errors. One hundred MC runs are implemented for case I, and the corresponding ASTD results when $\lambda = 10^{-5}$ and $\lambda = 10^{-4}$ are listed in Table 11 and Table 12, respectively. Re-note that the results in Table 11 and Table 12 are in the HEI frame. As shown in Table 11 and Table 12, the estimated errors of both two methods (that is, with and without VBR measurements) increase when considering the ephemeris errors. However, noteworthy improvements can be found by adding VBR measurements. Taking the situation $\lambda = 10^{-5}$ as an example, when using one VBR measurement, the averaged STDs along the x-, y-, and z-axes decrease by 42.06%, 44.65%, and 44.52%, respectively, whereas when using five VBR measurements, the averaged STDs along the three axes are reduced by 58.50%, 62.28%, and 62.07%, respectively.

Table 11 ASTD results of case I considering ephemeris errors ($\lambda = 10^{-5}$)

Methods	n_{VBR}	Position (km)			Velocity (km/s)		
		x	y	z	$\dot{x}$	$\dot{y}$	$\dot{z}$
Angle only	0	18.8980	134.3115	45.3375	0.1891	1.2581	0.4432
Angle and VBR	1	10.9487	74.3289	25.1524	0.0812	0.4385	0.1706
	5	7.8424	50.6492	17.1932	0.0450	0.1628	0.0777

Note that the intent of this simulation is to demonstrate the proposed method's capacity for improving OD performance in the presence of ephemeris errors. In practice, the ephemeris errors of the asteroid can be handled using cooperative OD techniques, in which the orbits of both the spacecraft and the asteroid are estimated simultaneously.

Table 12 ASTD results of case I considering ephemeris errors ($\lambda = 10^{-4}$)

Methods	n_{VBR}	Position (km)			Velocity (km/s)		
		x	y	z	$\dot{x}$	$\dot{y}$	$\dot{z}$
Angle only	0	20.0281	140.1841	47.3595	0.1753	1.1973	0.4190
Angle and VBR	1	14.8367	99.3538	33.6441	0.0870	0.4821	0.1777
	5	10.3991	66.7698	22.6712	0.0517	0.1991	0.0878

V. Conclusion

Valid vision-based range (VBR) information can be obtained by calculating the asteroid's area projected on the image plane and generating range ratio data. Numerical simulations show that the range ambiguity problem of the conventional angle-only orbit determination (OD) system can be solved using the proposed VBR measurements. The OD errors are reduced by at least 37.59%, and the convergence performances can be significantly improved using the proposed method. Noteworthy improvements in estimated accuracy for the asteroid approach OD can be achieved if the number of the VBR measurements used increases or the initial estimation uncertainties are larger; however, they also lead to a poorer uncertainty quantification capability of the filter algorithm. Additionally, sensitivity analysis results show that the proposed method outperforms the conventional angle-only OD approach in the presence of ephemeris errors.

Acknowledgments

This research was funded by the National Natural Science Foundation of China (No. 62394353, No. 12150008). The authors also thank Yuepeng Liu for the helpful discussion.

References

[1] Hawkins, S. E., Darlington, E. H., Murchie, S. L., et al., "Multi-Spectral Imager on the Near Earth Asteroid Rendezvous Mission," *Space Science Reviews*, Vol. 82, No. 1, 1997, pp. 31–100. https://doi.org/10.1023/A:1005099211710.

[2] Kuppa, K., McMahon, J. W., and Dietrich, A. B., "Initial Pole Axis and Spin Direction Estimation of Asteroids Using Infrared Imagery," *Journal of Guidance, Control, and Dynamics*, Vol. 47, No. 6, 2024, pp. 1055–1071. https://doi.org/10.2514/1.G007736.

[3] Li, X., Qiao, D., and Jia, F., "Investigation of Stable Regions of Spacecraft Motion in Binary Asteroid Systems by Terminal Condition Maps," *The Journal of the Astronautical Sciences*, Vol. 68, No. 4, 2021, pp. 891–915. https://doi.org/10.1007/s40295-021-00296-7.

[4] Carruba, V., Aljbaae, S., Domingos, R. C., et al., "Machine learning applied to asteroid dynamics," *Celestial Mechanics and Dynamical Astronomy*, Vol. 134, No. 4, 2022, p. 36. https://doi.org/10.1007/s10569-022-10088-2.

[5] Zhao, Y., Yang, H., Li, S., et al., "On-board modeling of gravity fields of elongated asteroids using Hopfield neural networks," *Astrodynamics*, Vol. 7, No. 1, 2023, pp. 101–114. https://doi.org/10.1007/s42064-022-0151-3.

[6] Hu, R., Huang, X., and Xu, C., "Integrated visual navigation based on angles-only measurements for asteroid final landing phase," *Astrodynamics*, Vol. 7, No. 1, 2023, pp. 69–82. https://doi.org/10.1007/s42064-022-0143-3.

[7] Prockter, L., Murchie, S., Cheng, A., et al., "The NEAR shoemaker mission to asteroid 433 eros," *Acta Astronautica*, Vol. 51, No. 1, 2002, pp. 491–500. https://doi.org/10.1016/S0094-5765(02)00098-X.

[8] Watanabe, S.-i., Tsuda, Y., Yoshikawa, M., et al., "Hayabusa2 Mission Overview," *Space Science Reviews*, Vol. 208, No. 1, 2017, pp. 3–16. https://doi.org/10.1007/s11214-017-0377-1.

[9] Lauretta, D. S., Balram-Knutson, S. S., Beshore, E., et al., "OSIRIS-REx: Sample Return from Asteroid (101955) Bennu," *Space Science Reviews*, Vol. 212, No. 1, 2017, pp. 925–984. https://doi.org/10.1007/s11214-017-0405-1.

[10] Williams, B., Antreasian, P., Carranza, E., et al., "OSIRIS-REx Flight Dynamics and Navigation Design," *Space Science Reviews*, Vol. 214, No. 4, 2018, p. 69. https://doi.org/10.1007/s11214-018-0501-x.

[11] Cheng, A. F., Atchison, J., Kantsiper, B., et al., "Asteroid Impact and Deflection Assessment mission," *Acta Astronautica*, Vol. 115, 2015, pp. 262–269. https://doi.org/10.1016/j.actaastro.2015.05.021.

[12] Chabot, N. L., Rivkin, A. S., Cheng, A. F., et al., "Achievement of the Planetary Defense Investigations of the Double Asteroid Redirection Test (DART) Mission," *The Planetary Science Journal*, Vol. 5, No. 2, 2024, p. 49. https://doi.org/10.3847/PSJ/ad16e6.

[13] Takahashi, S., and Scheeres, D. J., "Autonomous Exploration of a Small Near-Earth Asteroid," *Journal of Guidance, Control, and Dynamics*, Vol. 44, No. 4, 2021, pp. 701–718. https://doi.org/10.2514/1.G005733.

[14] Machuca, P., and Sánchez, J.-P., "CubeSat Autonomous Navigation and Guidance for Low-Cost Asteroid Flyby Missions," *Journal of Spacecraft and Rockets*, Vol. 58, No. 6, 2021, pp. 1858–1875. https://doi.org/10.2514/1.A34986.

[15] Li, S., and Cui, P., "Landmark tracking based autonomous navigation schemes for landing spacecraft on asteroids," *Acta Astronautica*, Vol. 62, No. 6, 2008, pp. 391–403. https://doi.org/10.1016/j.actaastro.2007.11.009.

[16] McCarthy, L. K., Adam, C. D., Leonard, J. M., et al., "OSIRIS-REx Landmark Optical Navigation Performance During Orbital and Close Proximity Operations at Asteroid Bennu," *AIAA SCITECH 2022 Forum*, AIAA SciTech Forum, American Institute of Aeronautics and Astronautics, 2021. https://doi.org/doi:10.2514/6.2022-2520.

[17] Ge, D., Cui, P., and Zhu, S., "Recent development of autonomous GNC technologies for small celestial body descent and landing," *Progress in Aerospace Sciences*, Vol. 110, 2019, p. 100551. https://doi.org/10.1016/j.paerosci.2019.06.002.

[18] Li, X., Scheeres, D. J., and Qiao, D., "Bouncing Return Trajectory Design for Precise Lander Deployment to Asteroids," *Journal of Guidance, Control, and Dynamics*, Vol. 45, No. 1, 2021, pp. 121–137. https://doi.org/10.2514/1.G006016.

[19] Qiao, D., Zhou, X., Zhao, Z., et al., "Asteroid Approaching Orbit Optimization Considering Optical Navigation Observability," *IEEE Transactions on Aerospace and Electronic Systems*, Vol. 58, No. 6, 2022, pp. 5165–5179. https://doi.org/10.1109/TAES.2022.3167653.

[20] Casini, S., Cervone, A., Monna, B., et al., "On line-of-sight navigation for deep-space applications: A performance analysis," *Advances in Space Research*, Vol. 72, No. 7, 2023, pp. 2994–3008. https://doi.org/10.1016/j.asr.2022.12.017.

[21] Zhou, X., Qin, T., Macdonald, M., et al., "Observability analysis of cooperative orbit determination using inertial inter-spacecraft angle measurements," *Acta Astronautica*, Vol. 210, 2023, pp. 289–302. https://doi.org/10.1016/j.actaastro.2023.05.019.

[22] Andreis, E., Franzese, V., and Topputo, F., "Onboard Orbit Determination for Deep-Space CubeSats," *Journal of Guidance, Control, and Dynamics*, Vol. 45, No. 8, 2022, pp. 1466–1480. https://doi.org/10.2514/1.G006294.

[23] Sun, Q., Gutiérrez, J. L. R., and Yu, X., "Deep Neural Network-Based 4-Quadrant Analog Sun Sensor Calibration," *Space: Science & Technology*, Vol. 3, 2023, p. 24. https://doi.org/10.34133/space.0024.

[24] Gong, B., Wang, S., Li, S., et al., "Review of space relative navigation based on angles-only measurements," *Astrodynamics*, Vol. 7, No. 2, 2023, pp. 131–152. https://doi.org/10.1007/s42064-022-0152-2.

[25] Li, R., Sun, C., Yu, X., et al., "Space Noncooperative Target Trajectory Tracking Based on Maneuvering Parameter Estimation," *Space: Science & Technology*, Vol. 3, 2024, p. 78. https://doi.org/10.34133/space.0078.

[26] Zhou, X., Li, X., Huo, Z., et al., "Near-Earth Asteroid Surveillance Constellation in the Sun-Venus Three-Body System," *Space: Science & Technology*, Vol. 2022, 2022, p. 9864937. https://doi.org/10.34133/2022/9864937.

[27] Du, R., Liao, W., and Zhang, X., "Feasibility analysis of angles-only navigation algorithm with multisensor data fusion for spacecraft noncooperative rendezvous," *Astrodynamics*, Vol. 7, No. 2, 2023, pp. 179–196. https://doi.org/10.1007/s42064-022-0148-y.

[28] Dietrich, A., and McMahon, J. W., "Asteroid Proximity Navigation using Flash LIDAR," *AIAA/AAS Astrodynamics Specialist Conference*, AIAA SPACE Forum, American Institute of Aeronautics and Astronautics, 2014. https://doi.org//10.2514/6.2014-4355.

[29] Ou, Y., Zhang, H., and Li, B., "Absolute orbit determination using line-of-sight vector measurements between formation flying spacecraft," *Astrophysics and Space Science*, Vol. 363, No. 4, 2018, p. 76. https://doi.org/10.1007/s10509-018-3293-2.

[30] Christian, J. A., "Optical Navigation Using Planet's Centroid and Apparent Diameter in Image," *Journal of Guidance, Control, and Dynamics*, Vol. 38, No. 2, 2014, pp. 192–204. https://doi.org/10.2514/1.G000872.

[31] Pedros-Faura, A., and McMahon, J. W., "Mixed Fidelity Shape Models for Efficient Small Body Gravity Modeling," *Journal of Guidance, Control, and Dynamics*, Vol. 47, No. 2, 2023, pp. 247–261. https://doi.org/10.2514/1.G007617.

[32] Torre, F., Grey, S., and Vasile, M., "Angles-Only Navigation in the Proximity of a Binary Asteroid System," *Journal of Guidance, Control, and Dynamics*, Vol. 44, No. 1, 2020, pp. 57–74. https://doi.org/10.2514/1.G004355.

[33] Folkner, W. M., Williams, J. G., Boggs, D. H., et al., "The planetary and lunar ephemerides DE430 and DE431," *Interplanetary Network Progress Report*, Vol. 196, 2014, pp. 42–196.

[34] Liounis, A., Swenson, J., Small, J., et al., "Independent Optical Navigation Processing for the Osiris-Rex Mission Using the Goddard Image Analysis and Navigation Tool," *2nd Annual RPI Workshop on Image-Based Modeling and Navigation for Space Applications*, Saratoga Springs, NY, United States, 2019.

[35] Jiang, Y., and Baoyin, H., "Robust extended Kalman filter with input estimation for maneuver tracking," *Chinese Journal of Aeronautics*, Vol. 31, No. 9, 2018, pp. 1910–1919. https://doi.org/10.1016/j.cja.2018.06.014.

[36] Yan, H., Liu, H., Sun, X., et al., "Accuracy Evaluation of Marginalized Unscented Kalman Filter," *Space: Science & Technology*, Vol. 3, 2024, p. 85. https://doi.org/10.34133/space.0085.

[37] Liu, Y., Zhang, X., Qiao, D., et al., "Improved subpixel edge detection for asteroid approach process images with Zernike moments," *SCIENTIA SINICA Technologica*, Vol. 54, No. 8, 2024, pp. 1473–1484. https://doi.org/10.1360/SST-2023-0321.

[38] Honarvar Shakibaei Asli, B., Flusser, J., Zhao, Y., et al., "Filter-generating system of Zernike polynomials," *Automatica*, Vol. 108, 2019, p. 108498. https://doi.org/10.1016/j.automatica.2019.108498.

[39] Christian, J. A., "Accurate Planetary Limb Localization for Image-Based Spacecraft Navigation," *Journal of Spacecraft and Rockets*, Vol. 54, No. 3, 2017, pp. 708–730. https://doi.org/10.2514/1.A33692.

[40] McCabe, J. S., and DeMars, K. J., "Anonymous Feature-Based Terrain Relative Navigation," *Journal of Guidance, Control, and Dynamics*, Vol. 43, No. 3, 2019, pp. 410–421. https://doi.org/10.2514/1.G004423.

[41] Zhou, X., "Software: Optical Navigation Using Vision-Based Range Measurements (v1.0.1)," *Zenodo*, 2024. https://doi.org/10.5281/zenodo.11227997.

[42] Dormand, J. R., and Prince, P. J., "A family of embedded Runge-Kutta formulae," *Journal of Computational and Applied Mathematics*, Vol. 6, No. 1, 1980, pp. 19–26. https://doi.org/10.1016/0771-050X(80)90013-3.

[43] Antreasian, P. G., Moreau, M. C., Adam, C. D., et al., "Early navigation performance of the OSIRIS-REx approach to Bennu," *42nd AAS Rocky Mountain Section Guidance and Control Conference*, Advances in the Astronautical Sciences, 2019, pp. 141–160.

[44] Adam, C. D., Knutson, S., Billett, O., et al., "Concept of Operations for OSIRIS-REx Optical Navigation Image Planning," *AIAA SCITECH 2022 Forum*, AIAA SciTech Forum, American Institute of Aeronautics and Astronautics, 2021. https://doi.org/doi:10.2514/6.2022-1569.

[45] Zhang, Y., Tian, X., and Ren, P., "An adaptive bilateral filter based framework for image denoising," *Neurocomputing*, Vol. 140, 2014, pp. 299–316. https://doi.org/10.1016/j.neucom.2014.03.008.

[46] Zhou, X., Qiao, D., and Macdonald, M., "Orbit Determination for Impulsively Maneuvering Spacecraft Using Modified State Transition Tensor," *Journal of Guidance, Control, and Dynamics*, Vol. 47, No. 5, 2024, pp. 822–839. https://doi.org/10.2514/1.G007814.

[47] Park, R. S., and Scheeres, D. J., "Nonlinear semi-analytic methods for trajectory estimation," *Journal of Guidance, Control, and Dynamics*, Vol. 30, No. 6, 2007, pp. 1668–1676. https://doi.org/10.2514/1.29106.

[48] Valli, M., Armellin, R., di Lizia, P., et al., "Nonlinear filtering methods for spacecraft navigation based on differential algebra," *Acta Astronautica*, Vol. 94, No. 1, 2014, pp. 363–374. https://doi.org/10.1016/j.actaastro.2013.03.009.